

# PDMS-SILVER NANOCOMPOSITE FOR BENDABLE AND STRETCHABLE CONDUCTIVE STRIPES



A Thesis Submitted in Partial Fulfillment of the Requirements  
for the Degree of Master of Science in Petrochemistry and Polymer  
Science

Field of Study of Petrochemistry and Polymer Science

Faculty of Science

Chulalongkorn University

Academic Year 2018

Copyright of Chulalongkorn University

พีดีเอ็มเอส-ซิลเวอร์นาโนคอมพอสิตสำหรับแถบนำไฟฟ้าชนิดโค้งงอและยึดได้



วิทยานิพนธ์นี้เป็นส่วนหนึ่งของการศึกษาตามหลักสูตรปริญญาวิทยาศาสตรมหาบัณฑิต  
สาขาวิชาปิโตรเคมีและวิทยาศาสตร์พอลิเมอร์ สาขาวิชาปิโตรเคมีและวิทยาศาสตร์พอลิเมอร์

คณะวิทยาศาสตร์ จุฬาลงกรณ์มหาวิทยาลัย

ปีการศึกษา 2561

ลิขสิทธิ์ของจุฬาลงกรณ์มหาวิทยาลัย

Thesis Title	PDMS-SILVER NANOCOMPOSITE FOR BENDABLE AND STRETCHABLE CONDUCTIVE STRIPES
By	Miss Porapak Suriya
Field of Study	Petrochemistry and Polymer Science
Thesis Advisor	Professor Sanong Ekgasit, Ph.D.
Thesis Co Advisor	Jariya Buajarern, Ph.D.

---

Accepted by the Faculty of Science, Chulalongkorn University in Partial  
Fulfillment of the Requirement for the Master of Science

..... Dean of the Faculty of Science  
(Professor POLKIT SANGVANICH, Ph.D.)

#### THESIS COMMITTEE

..... Chairman  
(Assistant Professor Warinthorn Chavasiri, Ph.D.)  
..... Thesis Advisor  
(Professor Sanong Ekgasit, Ph.D.)  
..... Thesis Co-Advisor  
(Jariya Buajarern, Ph.D.)  
..... Examiner  
(Prasit Pattanuwat, Ph.D.)  
..... External Examiner  
(Assistant Professor Toemsak Srihirin, Ph.D.)

จุฬาลงกรณ์มหาวิทยาลัย  
CHULALONGKORN UNIVERSITY

กรรภัค สุริยะ : พีดีเอ็มเอส-ซิลเวอร์นาโนคอมพอสิตสำหรับแถบนำไฟฟ้าชนิดโค้งงอและยืดได้. ( PDMS-SILVER NANOCOMPOSITE FOR BENDABLE AND STRETCHABLE CONDUCTIVE STRIPES) อ.ที่ปรึกษาหลัก : ศ. ดร.สนอง เอกสิทธิ์, อ.ที่ปรึกษาร่วม : ดร.จริยา บัวเจริญ

งานวิจัยนี้สนใจพัฒนาการขึ้นรูปแถบนำไฟฟ้ายืดหยุ่นที่ประกอบด้วยฟิล์ม โลหะเงินที่มีรูพรุนฝังอยู่บนพื้นผิวของพอลิเมอร์ด้วยวิธีที่ง่าย สะดวก และประหยัด โดยใช้ซิลเวอร์อะซีเตตที่สังเคราะห์เองซึ่งมีโครงสร้างเป็นแท่ง จากนั้นถูกสลายด้วยทางความร้อนที่อุณหภูมิ 300 องศาเซลเซียส เพื่อเปลี่ยนเป็นฟิล์มโลหะเงินที่มีรูพรุนซึ่งนำไฟฟ้าได้ โดยโครงสร้างฟิล์มโลหะเงินที่มีรูพรุนประกอบด้วยอนุภาคเงินที่ผืนึกและหลอมรวมตัวกันเกิดเป็นโครงสร้างที่แข็ง ซึ่งโครงสร้างที่แข็งนั้นสามารถแตกหักได้ง่ายเมื่อให้แรงกับแถบนำไฟฟ้าและส่งผลทำให้ประสิทธิภาพในการนำไฟฟ้าลดลง ดังนั้นเพื่อลดการผืนึกและหลอมรวมตัวกันของอนุภาคเงิน พอลิโคมทิลไฮลอคเซนเบสหรือพีดีเอ็มเอสเหลวถูกใช้ในการเคลือบเป็นฟิล์มบางบนผิวของแท่งซิลเวอร์อะซีเตตขณะสลายด้วยทางความร้อน ผลการทดลองบ่งชี้ว่าอนุภาคเงินมีขนาดเล็กลงจาก ~950 นาโนเมตร เป็น ~240 นาโนเมตร ซึ่งแสดงให้เห็นว่าอนุภาคเงินในโครงสร้างฟิล์มโลหะเงินที่มีรูพรุนลดการรวมตัวกัน รวมถึงลดความแข็งและการแตกภายในโครงสร้างเมื่อให้แรงกับแถบนำไฟฟ้า ซึ่งในงานวิจัยนี้ทดสอบประสิทธิภาพในการนำไฟฟ้าของแถบนำไฟฟ้ายืดหยุ่นโดยการยืด โค้งงอ และบิด พบว่าฟิล์มโลหะเงินที่มีรูพรุนที่ถูกเคลือบด้วยพีดีเอ็มเอสเบส ให้ค่าการนำไฟฟ้าที่ดีกว่าฟิล์มโลหะเงินที่มีรูพรุนที่ไม่ได้ถูกเคลือบด้วยพีดีเอ็มเอสเบส และงานวิจัยนี้ยังนำเสนอการประยุกต์ใช้แถบนำไฟฟ้าเป็นเซ็นเซอร์ยืดหยุ่นสำหรับควบคุมการเคลื่อนไหวของแขนหุ่นยนต์อีกด้วย

จุฬาลงกรณ์มหาวิทยาลัย  
CHULALONGKORN UNIVERSITY

สาขาวิชา      ปีโคโรเคมีและวิทยาศาสตร์พอลิเมอร์  
ปีการศึกษา    2561

ลายมือชื่อนิสิต .....  
ลายมือชื่อ อ.ที่ปรึกษาหลัก .....  
ลายมือชื่อ อ.ที่ปรึกษาร่วม .....

# # 5972034423 : MAJOR PETROCHEMISTRY AND POLYMER SCIENCE

KEYWORD silver acetate, porous silver film

D:

Porapak Suriya : PDMS-SILVER NANOCOMPOSITE FOR BENDABLE AND STRETCHABLE CONDUCTIVE STRIPES. Advisor: Prof. Sanong Ekgasit, Ph.D. Co-advisor: Jariya Buajarern, Ph.D.

In this research, a simple and low-cost protocol for fabricating PDMS-silver composite as flexible conductive polymer is presented. Rod-shaped silver acetate (RS-AcOAg) was synthesized and fabricated into a solvent-cast RS-AcOAg film. The film was thermally decomposed into porous silver structures at 300°C. The thermal decomposition of RS-AcOAg film induced the formation of silver microparticles (AgNPs) on the surface of RS-AcOAg with the expense of RS-AcOAg rod. AgNPs sintered into bigger particles and turned RS-AcOAg film into porous silver film consisting of interconnected quasi-sphere silver microparticles (AgMPs). The sintered structures transformed porous silver into rigid structures and affected the electrical resistivity due to the cracked structures when mechanical strain was applied. To suppress the sintering of the AgMPs, polydimethylsiloxane base (bPDMS) was coated on the surface of RS-AcOAg before the thermal decomposition. The bPDMS decreased mobility of AgMPs and suppressed the sintering. The porous silver film with and without bPDMS-suppressed sintering consisted of AgMPs with particle size of ~240 nm and ~950 nm, respectively. Commercial columnar silver acetate (CC-AcOAg) was employed for comparison purpose. The porous silver film with bPDMS-suppressed sintering strongly embedded onto the surface of polydimethylsiloxane (PDMS) as PDMS-silver composite, exhibited excellent mechanical properties with high conductivity under mechanical strain, including stretching, bending, and twisting. An application of PDMS-silver composite as a flexible conductive strip to use as strain sensor for robotic hand was demonstrated.

จุฬาลงกรณ์มหาวิทยาลัย  
CHULALONGKORN UNIVERSITY

Field of Study: Petrochemistry and  
Polymer Science

Academic 2018

Year:

Student's Signature

.....

Advisor's Signature

.....

Co-advisor's Signature

.....

## ACKNOWLEDGEMENTS

I would like to express my sincere gratitude to my thesis advisor, Professor Dr. Sanong Egkasit for providing the supporting, suggestions, motivation, training and understanding as well as patiently practices my technical skill during the whole research.

I would like to thank Dr. Jariya Buajarern, Assistant Professor Dr. Warinthorn Chavasiri, Dr. Prasit Pattanuwat, Assistant Professor Dr. Toemsak Srihirin for being my thesis committee with thoughtful and useful suggestions.

Above all, I am proudly grateful to my family for all their loves, supports, and encouragement throughout my graduate study.

Porapak Suriya

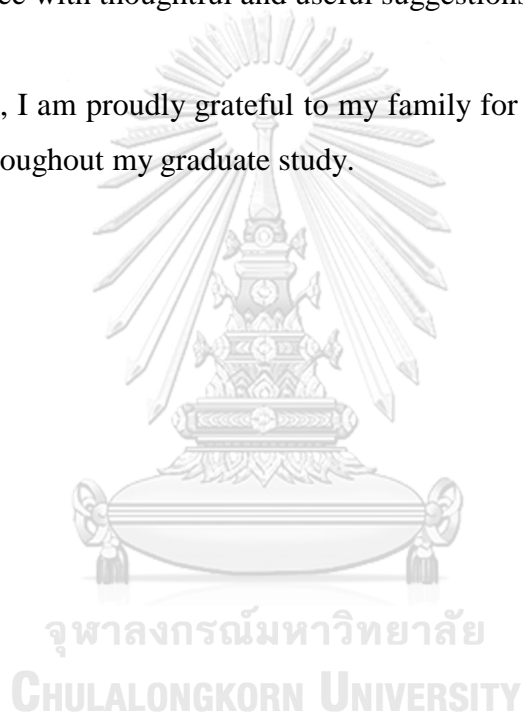


# TABLE OF CONTENTS

	<b>Page</b>
.....	iii
ABSTRACT (THAI) .....	iii
.....	iv
ABSTRACT (ENGLISH) .....	iv
ACKNOWLEDGEMENTS .....	v
TABLE OF CONTENTS .....	vi
LIST OF TABLES .....	ix
LIST OF FIGURES .....	x
LIST OF SYMBOLS AND ABBREVIATIONS .....	xiv
CHAPTER I INTRODUCTION.....	1
1.1 The objectives.....	2
1.2 Scopes of research .....	2
CHAPTER II THEORETICAL BACKGROUND .....	3
2.1 Flexible conductive polymer .....	3
2.1.1 Applications of flexible conductive polymer .....	3
2.2 Silver acetate (AcOAg).....	6
2.2.1 Synthesis of silver acetate .....	7
2.2.2 Thermal decomposition of silver acetate.....	7
2.2.3 Applications of AcOAg.....	10
2.3 Sintering effect.....	11
2.3.1 Sintering resistance.....	11
2.4 Polydimethylsiloxane (PDMS) .....	11
2.4.1 The structure of PDMS.....	12
2.4.2 The properties of PDMS.....	13
2.4.2.1 The physical properties of PDMS elastomeric polymer.....	13

2.4.2.2 The chemical properties of PDMS .....	14
2.4.2.3 The mechanical properties of PDMS .....	14
2.4.2.4 The thermal properties of PDMS .....	14
2.4.3 Applications of PDMS polymer .....	15
CHAPTER III EXPERIMENTAL SECTION.....	16
3.1 Chemical reagents .....	16
3.2 Instruments .....	16
3.3 Synthesis of rod-shaped silver acetate (RS-AcOAg) .....	17
3.4 Preparation of porous silver films with and without polydimethylsiloxane base (bPDMS) film coating .....	17
3.5 Fabrication of porous silver films as flexible conductive strips.....	18
3.6 Characterization the morphology of silver acetate and porous silver films .....	19
3.6.1 Scanning Electron Microscopy (SEM).....	19
3.6.2 Optical microscopy (OM) .....	20
3.7 Characterization of molecular information of the silver acetate before and after thermal decomposition .....	20
3.7.1 Fourier-transform infrared spectroscopy.....	20
3.7.2 Raman spectroscopy.....	20
3.8 Characterization of diffraction pattern of silver acetate .....	20
3.8.1 X-ray diffraction.....	20
3.9 Study of thermal properties of silver acetate and porous silver films .....	21
3.9.1 Thermal gravimetric analysis (TGA) .....	21
3.9.2 Differential Scanning Calorimetry (DSC).....	21
3.10 Study of surface area of porous silver films.....	21
3.11 Electrical resistance measurement of porous silver conductive strip.....	21
CHAPTER IV RESULTS AND DISCUSSION.....	23
4.1 Synthesis of RS-AcOAg.....	23
4.2 Morphology of RS-AcOAg .....	24
4.3 Comparison between RS-AcOAg and CC-AcOAg.....	25
4.3.1 Dimensions.....	25



4.3.2 Molecular information.....	26
4.3.3 Thermal decomposition.....	28
4.3.4 Thermal dependence decomposition and sintered structures.....	30
4.3.5 Suppressed sintering porous silver structure by bPDMS.....	34
4.4 Comparison of RS-AcOAg and CC-AcOAg after coating with bPDMS.....	38
4.4.1 Thermal decomposition.....	38
4.4.2 Thermal dependence decomposition and suppressed sintering.....	42
4.4.3 The morphology of porous silver structures.....	45
4.4.4 The morphology of microparticles (AgMPs).....	46
4.4.5 The surface areas of porous silver structures.....	48
4.4.6 Elemental analysis.....	49
4.5 Fabrication of PDMS-silver composite flexible conductive strips.....	52
CHAPTER V CONCLUSIONS.....	60
REFERENCES.....	62
VITA.....	71

## LIST OF TABLES

Table 2.1 The fabrication of flexible conductive material and its applications.....	5
Table 2.2 The general information of silver acetate [50].....	7
Table 2.3 The physical properties of PDMS SYLGARD® 184. ....	13
Table 4.1 Thermal properties of RS-AcOAg and CC-AcOAg.....	29
Table 4.2 Thermal properties of RS-AcOAg, bPDMS-coated RS-AcOAg, CC-AcOAg, and bPDMS-coated CC-AcOAg.....	40
Table 4.3 The surface areas of porous silver structures.....	49



## LIST OF FIGURES

Figure 2.1	Flexible conductive polymer [38].	3
Figure 2.2	Structure of silver acetate.	6
Figure 2.3	TGA-DTG thermograms obtained by heating the AcOAg (A) in air, and (B) nitrogen atmospheres with heating rate of $20^{\circ}\text{C min}^{-1}$ [49].	8
Figure 2.4	DSC curve for the decomposition of $\text{CH}_3\text{COOAg}$ ; $m=13.9$ mg, standard aluminum-sample holder (the lid with holes), heating rate $10\text{ K min}^{-1}$ , Ar flow ( $25\text{ cm}^3\text{ min}^{-1}$ ) [48].	9
Figure 2.5	SEM images of partially decomposed silver acetate obtained by heating the sample at different temperatures (a, b) = $180^{\circ}\text{C}$ , (c, d) = $195^{\circ}\text{C}$ , and (e, f) = $300^{\circ}\text{C}$ [45].	10
Figure 2.6	Sintering mechanism [54].	11
Figure 2.7	The chemical structure of PDMS repeating monomer units.	12
Figure 2.8	The chemical structure of PDMS base, SYLGARD <sup>®</sup> 184.	12
Figure 2.9	The chemical structure of PDMS curing agent, SYLGARD <sup>®</sup> 184.	12
Figure 2.10	Schematic represents the polymerization of PDMS, SYLGARD <sup>®</sup> 184.	13
Figure 2.11	TGA thermograms of PDMS ( $\text{N}_2$ , $10^{\circ}\text{Cmin}^{-1}$ ) [62].	14
Figure 3.1	The schematic represented a step of rod-shaped RS-AcOAg synthesis. .	17
Figure 3.2	Schematic represented the preparation of a porous film by using (A1) RS-AcOAg, (A2) CC-AcOAg, (B1) bPDMS-coated RS-AcOAg, and (B2) bPDMS-coated CC-AcOAg.	18
Figure 3.3	The fabrication of porous silver conductive strip from (A) RS-ACOAg and (B) bPDMS-coated RS-AcOAg.	19
Figure 3.4	The mechanical strain devices (A) stretching, (B) bending, (C) twisting for electrical resistivity measurement.	22
Figure 4.1	Digital photographs showing crystal growth of AcOAg.	23
Figure 4.2	The morphological growth of AcOAg crystals.	24
Figure 4.3	SEM micrographs of (A) Bun-AcOAg and (B) RS-AcOAg.	25
Figure 4.4	SEM micrographs of (A) RS-AcOAg and (B) CC-AcOAg and the corresponding size distribution of widths and lengths.	26

Figure 4.5 (A) FTIR spectra, (B) Raman spectra, and (C) XRD patterns of RS-AcOAg and CC-AcOAg. ....	27
Figure 4.6 TG and the corresponding DTG curves of (A) RS-AcOAg and (B) CC-AcOAg. ....	29
Figure 4.7 DSC thermograms of RS-AcOAg and CC-AcOAg. ....	30
Figure 4.8 Size distribution of AgMPs obtained by decomposition of (A) RS-AcOAg and (B) CC-AcOAg at 200°C, 250°C, and 300°C. ....	32
Figure 4.9 FTIR spectra of thermally decomposed (A) RS-AcOAg and (B) CC-AcOAg at RT, 200°C, 250°C, and 300°C. ....	33
Figure 4.10 TG thermogram of bPDMS. ....	34
Figure 4.11 Photographic images of (A) bPDMS-coated RS-AcOAg on glass substrates at room temperature and (B) thermally decomposed at 300°C at various amount of bPDMS: (1) bPDMS-free, (2) 0.001 g, (3) 0.003 g, (4) 0.005 g, (5) 0.01 g, and (6) 0.02 g. ....	35
Figure 4.12 SEM micrographs of (A) bPDMS-coated RS-AcOAg films on glass substrates at room temperature and (B) the corresponding thermally decomposed films at 300°C with various amount of bPDMS: (1) bPDMS-free, (2) 0.001 g, (3) 0.003 g, (4) 0.005 g, (5) 0.01 g, and (6) 0.02 g. ....	36
Figure 4.13 Digital photographs and the corresponding SEM micrographs of (A) porous silver from excess bPDMS-coated RS-AcOAg, and (B) A after rinsing by ethyl acetate. ....	37
Figure 4.14 TG thermograms and the corresponding DTG thermograms of (A1) RS-AcOAg, (A2) bPDMS-coated RS-AcOAg, (B1) CC-AcOAg, and (B2) bPDMS-coated CC-AcOAg. ....	39
Figure 4.15 TG thermograms of RS-AcOAg, bPDMS-coated RS-AcOAg, CC-AcOAg, and bPDMS-coated CC-AcOAg. ....	40
Figure 4.16 DSC profiles of RS-AcOAg, bPDMS-coated RS-AcOAg, CC-AcOAg and bPDMS-coated CC-AcOAg. ....	41
Figure 4.17 Size distribution of AgMPs obtained by decomposition of (A) bPDMS-coated RS-AgOAc and (B) bPDMS-coated CC-AgOAc at 200°C, 250°C, and 300°C. ....	43
Figure 4.18 FTIR spectra of thermal dependence decomposition of (A) bPDMS-coated RS-AcOAg and (B) bPDMS-coated CC-AcOAg at RT, 200°C, 250°C, and 300°C. ....	45

- Figure 4.19 SEM micrographs of the porous silver structures of (A1) RS-AcOAg, (A2) bPDMS-coated RS-AcOAg, (B1) CC-AOAg, and (B2) bPDMS-coated CC-AcOAg after thermal decomposition. ....46
- Figure 4.20 Size distribution histograms of AgMPs after thermal decomposition of (A1) RS-AgOAc, (A2) bPDMS-coated RS-AcOAg, (B1) CC-AgOAc, and (B2) bPDMS-coated RS-AcOAg. ....48
- Figure 4.21 SEM-EDX point analysis of (A) RS-AcOAg, (B) after thermally decomposed RS-AcOAg, (C) bPDMS-coated RS-AcOAg, and (D) after thermally decomposed bPDMS-coated RS-AcOAg. ....49
- Figure 4.22 SEM-EDX point analysis of (A) CC-AcOAg, (B) thermally decomposed CC-AcOAg, (C) bPDMS-coated CC-AcOAg, and (D) thermally decomposed bPDMS-coated CC-AcOAg. ....50
- Figure 4.23 Porous silver structure of (A) RS-AcOAg and (B) bPDMS-coated RS-AcOAg after thermal decomposition at 300°C. ....51
- Figure 4.24 (A) Digital images of hydrogen peroxide testing, confirming that silver structures were adhered on PDMS surface after fabrication. (B) LED light testing while the two-point probe multimeter was clipped on the surface of a strip. 52
- Figure 4.25 Optical microscope images of PDMS-silver composite as the porous silver strips from (A) RS-AcOAg and (B) bPDMS-coated RS-AcOAg; (Aa, Ba) original film ( $R=6.3 \Omega$ ,  $5.0 \Omega$ ), (Ab, Bb) during under strain ( $R=7.6 \Omega$ ,  $6.2 \Omega$ ), and (Ac, Bc) after releasing strain ( $R=7.0 \Omega$ ,  $5.0 \Omega$ ). The strips were under 30% strain. ....53
- Figure 4.26 Relative changes of electrical resistance ( $\Delta R/R_0$ ) under continuously applied the mechanical force with (A) stretching, (B) bending, and (C) twisting of flexible conductive strips. The blue, black, and red lines were represented the relative change of evaporated silver strip, porous silver strip from RS-AcOAg, and porous silver strip from bPDMS coated RS-AcOAg, respectively. ....55
- Figure 4.27 Relative changes of electrical resistance ( $\Delta R/R_0$ ) under cyclically applied mechanical loadings with (A) 30% strain, (B) 90° bending, and (C) 180° twisting of flexible conductive strips. The values for evaporated silver strip, porous silver strip from RS-AcOAg, and porous silver strip from bPDMS-coated RS-AcOAg are shown in blue, black, and red lines, respectively. ....57

- Figure 4.28 LED applications of porous silver conductive strip from bPDMS-coated RS-AcOAg. Photographic images of working LEDs under (A) 30% strain, (B) 90° bending, and (C) 180° twisting loads.....58
- Figure 4.29 The strain sensor fabricated from the porous silver strip of bPDMS-coated RS-AcOAg for controlling robotic arm movement. ....59



## LIST OF SYMBOLS AND ABBREVIATIONS

OM	optical microscope
CCD	charge-coupled device
SEM	scanning electron microscope
SEI	secondary electron imaging
EDS	energy-dispersive X-ray spectroscopy
TGA	thermal gravimetric analysis
DTG	derivative thermogravimetric analysis
DSC	differential scanning calorimetry
BET	Brunauer–Emmett–Teller
3D	three-dimension
PDMS	polydimethylsiloxane
bPDMS	polydimethylsiloxane base
AcOAg	silver acetate
RS-AcOAg	rod shaped-silver acetate
bPDMS-coated	polydimethylsiloxane base-coated
FS-AcOAg	flower shape silver acetate
Bun-AcOAg	bundle silver acetate
CC-AcOAg	commercial columnar silver acetate
bPDMS-coated	polydimethylsiloxane base-coated
PI	polyimide
°C	degree Celsius
RT	room temperature
LED	light-emitting diode
h	hour
min	minute
s	second
m	meter
mm	millimeter
μm	micrometer

nm	nanometer
cm <sup>-1</sup>	reciprocal centimeter
min <sup>-1</sup>	reciprocal minute
mol	mole
N	Newton
g	gram
mg	milligram
cm <sup>2</sup>	square centimeter
cm <sup>3</sup>	cubic centimeter
mL	milliliter
kV	kilovolt
mW	milliwatt
cps	count per second
S/m	siemens per meter
Ω	ohm
Ω/sq	ohms per square
K	kilo
M	mega
Pa	pascal
<i>N</i>	number of samples



# CHAPTER I

## INTRODUCTION

Due to their diverse potential applications, flexible conductive materials have attracted scientists' interest for decades [1-3]. The flexible conductive polymer is widely used for many electrical applications, including stretchable electrodes [4-5], medical device [6], and stretchable electronics [7-9] due to their excellent electrical properties under mechanical strain. (i.e., stretching, bending, and twisting).

Flexible conductive polymer is composed of a conductive material and a polymer substrate. Various conductive materials were successfully used in flexible conductive polymer fabrication including of silver [10-15], copper [16-17], carbon nanotube [18-19], and graphene [20-21]. Silver metal is widely employed for flexible conductive material fabrication due to its electrical conductivity ( $6.30 \times 10^5$  S/m at 20°C) [22]. For polymer substrates, polydimethylsiloxane (PDMS, SYLGARD® 184) [23-25], polyethylene terephthalate (PET) [26-27], and polyurethane (PU) [28] were commonly used for making flexible substrates due to a good elastic property under mechanical strain as bending [8]. Since past decade, several fabrication methods of flexible conductive polymer have been successfully accomplished, for example, screen printing [10, 12, 29-30], inkjet printing [11, 24, 31], spin coating [32-34], dip coating [14], and vacuum filtration [35].

In this research, the facile, simple, and low-cost fabrication method for PDMS-silver composite as flexible conductive strip was investigated. Rod-shaped silver acetate (RS-AcOAg) was synthesized and casted into a thin film via solvent-casting. The film was then thermally decomposed at 300°C to convert RS-AcOAg into silver microparticles (AgMPs) and sintered to form porous silver structures. The sintered-structures affect the electrical resistance of the strip because they form rigid porous silver structures, which are easily cracked [36]. To avoid sintering effect, polydimethylsiloxane base (bPDMS) is coating on RS-AcOAg surfaces which aims to suppress sintering. Then the mixture is casting into a film and thermal decomposition. The silver porous structures under suppress sintering are further fabricate into flexible conductive strips. The porous structures are strongly adhesive onto a surface of

PDMS by molding fabrication. The flexible conductive strip exhibited excellent mechanical properties and high conductivity under mechanical strains including stretching, bending, and twisting. Additionally, we demonstrated the potential to apply the flexible conductive strips as a strain sensor in robotic arms.

### **1.1 The objectives**

1. To synthesize rod-shaped silver acetate (RS-AcOAg).
2. To compare the properties of RS-AcOAg with commercial columnar silver acetate (CC-AcOAg).
3. To investigate porous silver films via thermal decomposition of RS-AcOAg and CC-AcOAg under polydimethylsiloxane base (bPDMS) suppressed sintering.
4. To fabricate the efficient flexible conductive strips by casting PDMS onto the porous silver films.
5. To demonstrate an application of the flexible conductive strips in strain sensor.

### **1.2 Scopes of research**

1. Develop the synthesis procedure of RS-AcOAg via ultra-sonication.
2. Compare the structure morphology, size distribution and chemical composition of silver acetate between homemade grade; RS-AcOAg and commercially available grade; CC-AcOAg.
3. Study the influence of bPDMS on the sintering effect of porous silver structures.
4. Study an electrical resistivity of porous silver strip under mechanical strain, stretching, bending, and twisting condition.
5. Demonstrate strain sensor by using porous silver strips in robotic arm.

## CHAPTER II

### THEORETICAL BACKGROUND

#### 2.1 Flexible conductive polymer

Flexible conductive polymer or commonly known as flex electronics (Figure 2.1) is mainly composed of conductive materials and polymer substrates. This material is a novel technology which is used for assembling electronic circuits by combined electronic devices on flexible polymer substrates. It can be folded, wrapped, rolled, and twisted with negligible effect on its electronic function [37].



Figure 2.1 Flexible conductive polymer [38].

##### 2.1.1 Applications of flexible conductive polymer

Yan Wang *et al.* demonstrated the preparation of flexible substrate for applying in flexible circuit of radio frequency identification (RFID) technology. In this work, a flexible substrate was fabricated based on functionalize stannous chloride ( $\text{SnCl}_2$ ) on a surface of Teslin paper. Then, a copper sheet which was a conductive material was printed on the top of modified-Teslin paper surface via electroless deposition techniques. The conductivity of fabricated substrate is up to  $4 \times 10^7$  S/m. Additionally, the conductivity of this substrate while applied the mechanical force (bending) was measured. The conductivity was decreased 4% and 9% when bend the substrate at  $90^\circ$  and  $180^\circ$ , respectively [39].

Jinhoon Kim *et al.* fabricated a highly stretchable transparent electrode by spin-coating a layer by layer of silver nanowire (AgNW), aerogel and polydimethylsiloxane (PDMS) on a glass substrate. After PDMS curing process, an

embedded AgNW-PDMS electrode was peeled of glass substrate. A sheet resistant ( $R_s$ ) was  $15 \Omega/\text{sq}$  and an optical transparency was 80%. In addition, a conductivity of this flexible electrode still maintained after stretched up to 70% for 100 cycles [33].

Jiazhen Sun *et al.* reported the fabrication method of bendable circuit board on PDMS surface. To form flexible substrate, PDMS sheet was firstly fabricated, then the mixture of trifluoroacetic acid and silver salt was printed onto the surface of PDMS sheet with strip pattern to form a flexible circuit board by inkjet printer. Further that, the silver salt was reduced into silver metal by hydrazine hydrate. The conductivity of flexible circuit board was measured using a platinum probe. The conductivity remained high even if the flexible circuit board was bended for 800 cycles [24].

Yougen Hu *et al.* fabricated flexible conductor by directly print on a substrate surface. The conductive paste was prepared by mix polystyrene (PS) and silver nitrate. Then, the paste was screen printed on PDMS sheet to fabricate flexible conductive polymer. The flexible conductive polymer was measured an electrical conductivity after 100 cycles and the electrical conductivity remained high [30].

Jun Young Jeon *et al.* presented flexible conductive polymer as electronics bandage for detecting joint movements. In this work, silver ink/CNT mixture was screen printed on the PDMS substrate. An electronics bandage gave high joint movement signal even it was under a 4% of strain [6].

Tallis Costa *et al.* studied a flexible sensor by using polyethylene terephthalate (PET) as a flexible substrate and carbon nanotube (CNT) as a conductive material. An inkjet printing was used for making a pattern of CNT on PET surface. The flexible sensor can absorb the forces with 0.5 N and an electrical resistivity increased only 21%. The flexible sensor was applied in stamp molding and BioMEMs [31].

Jinhui Li *et al.* presented flexible conductive polymer as electronics skin self-healing properties. Three-dimensional graphene structures with 2% of weight were mixed with furfurylamine (FAGS) for using as a self-healing agent. Polyurethane (PU) and bismaleimide were mixed into the FAGS mixture for making gel of flexible conductive polymer. The flexible conductive polymer remained an efficient electrical conductivity after 200 cycles of 10% strain [21].

Khushbu R. Zope *et al.* prepared silver ink from silver oxalate for applying in flexible conductive substrate fabrication. The silver ink can print onto various substrates such as PET, glasses, and polyimide (PI) to form flexible conductive substrates. Then, thermal-photonic curing was applied to make the silver ink attached on the substrates. The electrical resistivity of flexible conductive substrates was  $4.26 \times 10^{-8} \Omega\text{m}$  [15].

Table 2.1 The fabrication of flexible conductive material and its applications.

Year	Conductive Materials	Substrate Materials	Fabrication method	Application	Ref.
2016	Copper sheet	Teslin paper	Electroless deposition	Flexibles devices	[39]
2016	AgNWs	PDMS	Spin coating	Flexible electrode	[33]
2016	AgNPs	PDMS	Inkjet printing	Flexible circuit board	[24]
2016	AgNPs	PDMS	Screen printing	Flexible conductive	[30]
2016	Silver ink/CNT	PDMS	Screen printing	E-bandage	[6]
2017	CNT	PET	Inkjet printing	Flexible sensor	[31]
2018	Graphene	PU	Mixing	E-skin movement	[21]
2018	AgNPs	PET	Inkjet printing	Flexible conductive	[15]

Various kinds of conductive materials and flexible substrates were used in flexible conductive polymer fabrication (Table 2.1). Over the past 3 years, silver materials and PDMS substrates are commonly used in the fabrication process. With their unique property, flexible conductive polymer as composite materials can be applied in various applications.

## 2.2 Silver acetate (AcOAg)

Silver acetate (AcOAg) crystal is an inorganic compound which contained 8 membered ring structure (Figure 2.2) [40]. In general, AcOAg crystal is a white powder. It is a useful reagent in laboratory and industrial due to its water solubility and thermal decomposition temperature (Table 2.2). AcOAg is widely used worldwide, especially in America and Europe where it is an important ingredient in chewing gum and spray component for anti-smoking drug. Moreover, AcOAg can apply in many fields including, treating alcohol addiction [41]. In medical field, it has the potential to inhibit pathogens such as bacteria [42]. Focusing on an application in potential fabrication, AcOAg is used as silver coating [43] and conductive silver ink [44]. For chemical field, it is used as a precursor material for synthesizing silver microparticles (AgMPs) or silver nanoparticles (AgNPs) [45].

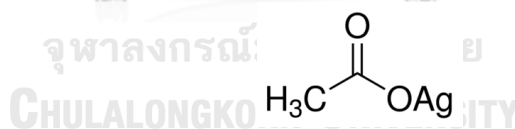


Figure 2.2 Structure of silver acetate.

Table 2.2 The general information of silver acetate [46].

Properties	Value
Chemical formula	$C_2H_3AgO_2$
Molecular mass	166.912 g/mol
Appearance	Solid, white powder
Decomposition temperature	280°C
Solubility	151 mg/mL in water at 25°C

### 2.2.1 Synthesis of silver acetate

Miller *et al.* used silver nitrate ( $AgNO_3$ ) as a precursor to synthesize silver acetate ( $AcOAg$ ) to use as silver coating. A 100 g of  $AgNO_3$  was dissolved in water. Then, an excess sodium hydroxide ( $NaOH$ ) was added into the solution to precipitate silver oxide ( $Ag_2O$ ). The 70 g of  $Ag_2O$  was obtained from the mixing solution. After that, mucilage or gum was added into the solution. Lastly, a 20 g of acetic acid ( $AcOH$ ) was added into the solution while stirring and ionized to acetate ions. Then, the acetate ions reacted with silver ion to form  $AcOAg$  [43].

Qadeer *et al.* prepared  $AcOAg$  from a reaction between  $AgNO_3$  and ammonium acetate ( $NH_4OAc$ ). Then,  $AcOAg$  powder was washed with DI water and left it dried at room temperature [47].

Logvinenko *et al.* prepared  $AcOAg$  by a reaction of acetic acid ( $AcOH$ ) and silver carbonate ( $Ag_2CO_3$ ) at 45-60°C. After that the reaction was cooled to room temperature to allow the white powder of  $AcOAg$  formation [48].

### 2.2.2 Thermal decomposition of silver acetate

To make the conductive material using  $AcOAg$ , thermal decomposition of  $AcOAg$  is required to convert  $AcOAg$  into porous silver metals because  $AcOAg$  itself is unable to be electrical conductivity. Chemical equations for thermal decomposition of  $AcOAg$  under  $O_2$  condition (Eq. 1) and inert gas condition (Eq. 2) are shown below [45].



To study thermal properties of AcOAg, thermogravimetric analysis (TGA) and derivative thermogravimetric analysis (DTG) were used as a tool for characterization up on heating AcOAg under thermal decomposition in air and nitrogen (Figure 2.3). The TGA-DTG profiles reveal similar thermal behavior in both air and nitrogen. The weight loss step maximized at 292°C and 295°C in air and nitrogen flow, respectively. This step resulted in residue values of 65.08 % (in air) and 64.20 % (in nitrogen) due to the loss of a mixture of CO, CO<sub>2</sub>, H<sub>2</sub>O and CH<sub>3</sub>COOH gases during the thermal decomposition of AcOAg [49].

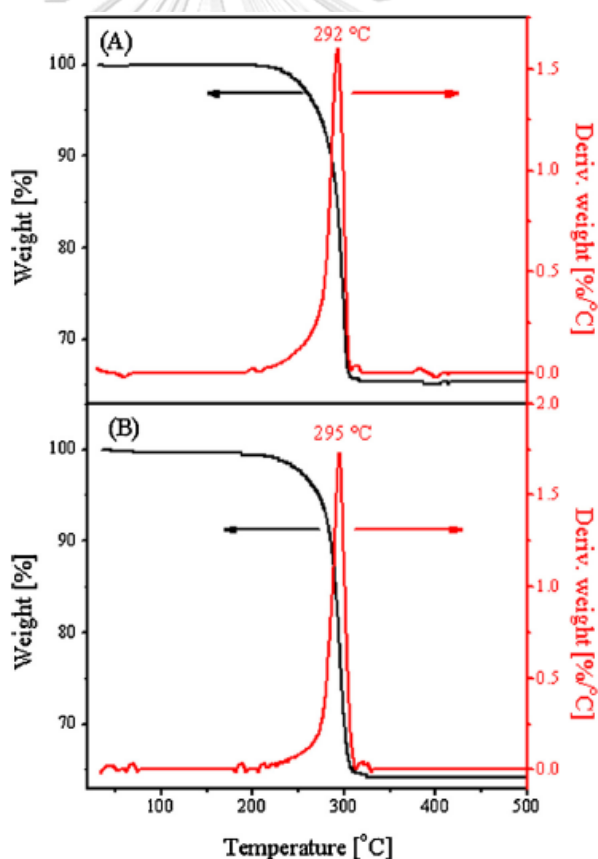


Figure 2.3 TGA-DTG thermograms obtained by heating the AcOAg (A) in air, and (B) nitrogen atmospheres with heating rate of 20°C min<sup>-1</sup> [49].



The differential scanning calorimetry (DSC) profile while decomposed AcOAg at 260-286°C with multi-steps and the long flat exothermic peak at 286-331°C referred to the fine recrystallization. Herein, the data referred to completely changed of physical and chemical properties at those temperatures (Figure 2.4) [48].

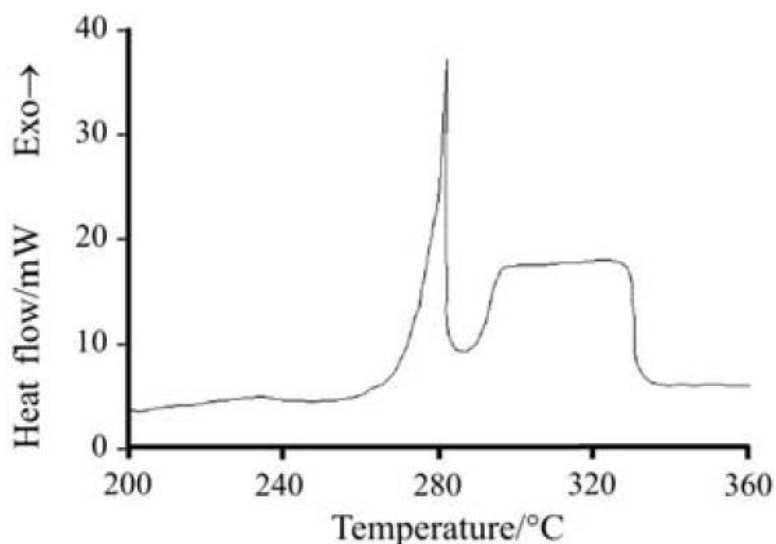


Figure 2.4 DSC curve for the decomposition of  $\text{CH}_3\text{COOAg}$ ;  $m=13.9$  mg, standard aluminum-sample holder (the lid with holes), heating rate  $10 \text{ K min}^{-1}$ , Ar flow ( $25 \text{ cm}^3 \text{ min}^{-1}$ ) [48].

To follow the changing of AcOAg structure after the thermal decomposition, SEM technique was used. The results show that the columnar AgOAc (Figure 2.5a) was thermally decomposed to a chain structure of AgNPs with sintering structures. While the columnar AcOAg was initially decomposed at  $180^\circ\text{C}$ , the spherical AgNPs with diameter 50 nm were formed along the columnar AcOAg surfaces (Figure 2.5b). When the temperature was heated up to  $195^\circ\text{C}$ , AgNPs were gradually aggregate and grow into submicron-sized particles at certain parts of the AcOAg surface (Figures 2.5 c and d). When the temperature raised up to  $300^\circ\text{C}$ , AgNPs aggregated and formed AgMPs as a chain along with the original columnar crystals of the AcOAg. The diameter of each AgMPs exhibited 250 nm (Figure 2.5f) [45].

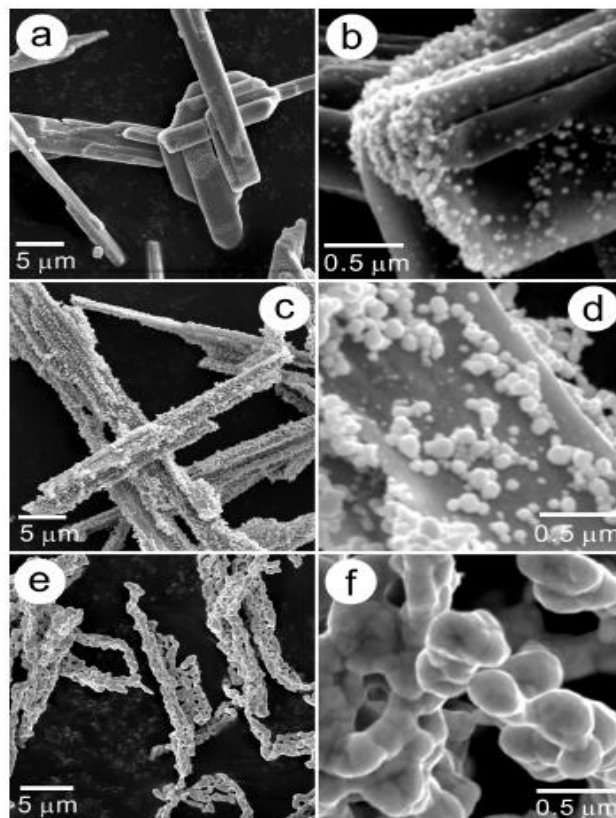


Figure 2.5 SEM images of partially decomposed silver acetate obtained by heating the sample at different temperatures (a, b) = 180°C, (c, d) = 195°C, and (e, f) = 300°C [45].

### 2.2.3 Applications of AcOAg

Due to the shape of AcOAg is a columnar crystal, it can form porous structures with high surface area, which is useful for using as electrical conductivity material and catalyst. Moreover, the low thermal decomposition temperature of AcOAg indicated that AcOAg can transform into silver metal with the low thermal energy.

Avellaneda *et al.* used AcOAg to inhibit the infectious disease of prosthetic parts and cardiac bypass surgery which can use for treat an obstructive coronary artery disease [50].

Jeanmonod *et al.* used AcOAg for coating of prosthetic vascular grafts improves their vascularization after implantation without inducing severe inflammatory side effects [51].

Tao *et al.* used AcOAg as a silver carrier for synthesizing of organic silver conductive ink (OSC ink). The OSC was printed on PDMS substrates for use as microelectronic devices [52].

### 2.3 Sintering effect

Sintering is the process of compacting and forming a solid structure of materials such as metals, ceramics, and plastics by thermal or pressure. The atoms of materials diffuse across the grain boundaries of particles, fusing and necking the particles together and creating the sintered structure [53]. In some cases, sintering is useful because it reduces the porosity and enhances properties such as strength, electrical conductivity, translucency and thermal conductivity. On the other hand, sintered structure is limiting the conductive properties such as the fabrication of forming flexible materials because it can break easily when apply mechanical strain.

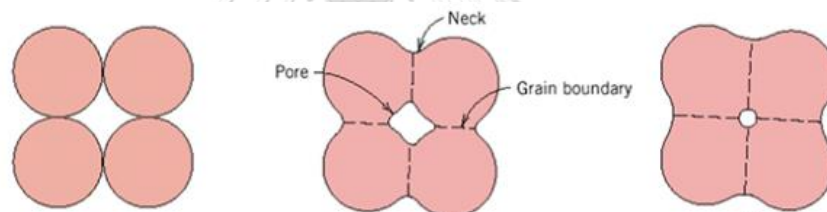


Figure 2.6 Sintering mechanism [54].

#### 2.3.1 Sintering resistance

The sintered structure can be controlled by adjusting temperature [55-56] or coating with surface stabilizing agent [57-59] to limit the diffusion of particles across the boundaries of atom which can prevent the fusing of particles to form the sintered structures. The rigid and the shrinkage of structures decreased after being control sintering.

### 2.4 Polydimethylsiloxane (PDMS)

Polydimethylsiloxane (PDMS) is polymeric organosilicon compounds that is based on silicone material. PDMS is colorless, transparent, hydrophobic, inert, flexible, non-toxic, and non-flammable. PDMS is widely used in industrial, consumer, food and medicinal or pharmaceutical applications [60].

### 2.4.1 The structure of PDMS

The chemical formula of PDMS monomer unit is  $(\text{CH}_3)_3\text{SiO}[\text{Si}(\text{CH}_3)_2\text{O}]_n(\text{CH}_3)_3$ , the repeating unit of PDMS polymer is  $[\text{Si}(\text{CH}_3)_2\text{O}]_n$  (Figure 2.7), where  $n$  is the number of repeating monomer units PDMS polymer possess 2 main compositions, PDMS base and PDMS curing agent. The chemical structure of PDMS base and curing agent are in Figure 2.8 and Figure 2.9, respectively. The polymerization was initiated when PDMS base and PDMS curing agent were mixed together as PDMS precursors. The  $-\text{Si}-\text{H}$  bond of PDMS curing agent was reacted with  $-\text{CH}=\text{CH}_2$  bond to form  $-\text{Si}-\text{CH}_2-\text{CH}_2-\text{Si}-$  as a cross-linked polymer or curing reaction (Figure 2.10). Generally, PDMS precursor are cured at  $60^\circ\text{C}$  for 30 minutes or at room temperature using 24 hours to form PDMS elastomeric polymer. Curing PDMS is an elastomeric material because it is soft texture and transparency [60].

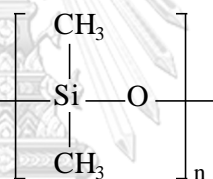


Figure 2.7 The chemical structure of PDMS repeating monomer units.

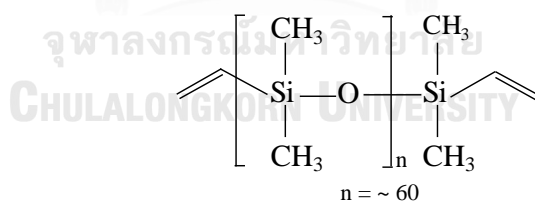


Figure 2.8 The chemical structure of PDMS base, SYLGARD® 184.

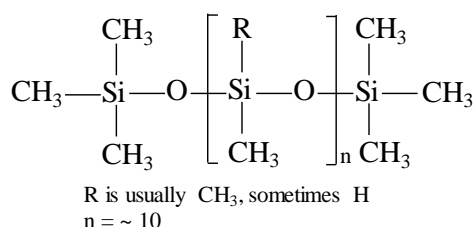


Figure 2.9 The chemical structure of PDMS curing agent, SYLGARD® 184.

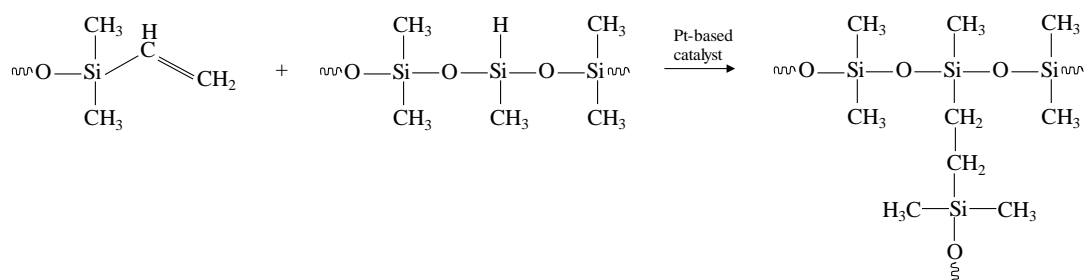


Figure 2.10 Schematic represents the polymerization of PDMS, SYLGARD<sup>®</sup> 184.

## 2.4.2 The properties of PDMS

### 2.4.2.1 The physical properties of PDMS elastomeric polymer

PDMS elastomeric polymer is colorless, transparency, hydrophobicity, inert, flexible, non-toxic, non-flammable, low glass transition temperature ( $T_g$ ) and crystalline melting temperature ( $T_m$ ). The service temperature range is  $-45^{\circ}\text{C}$  to  $200^{\circ}\text{C}$ . A general physical property of PDMS was presented in Table 2.3.

Table 2.3 The physical properties of PDMS SYLGARD<sup>®</sup> 184.

Properties	Value
Refractive Index	1.42
Viscosity base	5100 cP
Viscosity mixed	3500 cP
Specific Gravity	1.03
Shear modulus	411 KPa
Young's modulus	1.2 MPa
Yield strength	700 KPa
Glass transition temperature, $T_g$	$-125^{\circ}\text{C}$
Crystalline melting temperature, $T_m$	$-40^{\circ}\text{C}$

#### 2.4.2.2 The chemical properties of PDMS

PDMS elastomeric polymer is inert and hydrophobic, it does not react with chemical or organic solvents. PDMS elastomer polymer can be used with water and alcohol solvents without deformation. However, PDMS base can be dissolved in organic solvents, for example, ethyl acetate, toluene, and xylene.

#### 2.4.2.3 The mechanical properties of PDMS

PDMS elastomeric polymer is a viscoelastic material. After polymerization and cross-linking, it will be flexible and able to bend. As shown in Table 2.3, shear modulus and Young's modulus of PDMS elastomeric polymer are 411 KPa and 1.2 MPa, respectively [61].

#### 2.4.2.4 The thermal properties of PDMS

The thermal decomposition temperature of PDMS was proceed from 25°C to 800°C (Figure 2.9). C-Si bond was decomposed at 449.98°C. Si-O bond was decomposed at 546.85°C. The cyclic dimethyl siloxane bond was decomposed at 698.48°C The TGA thermograms of PDMS are presented in Figure 2.11 [62].

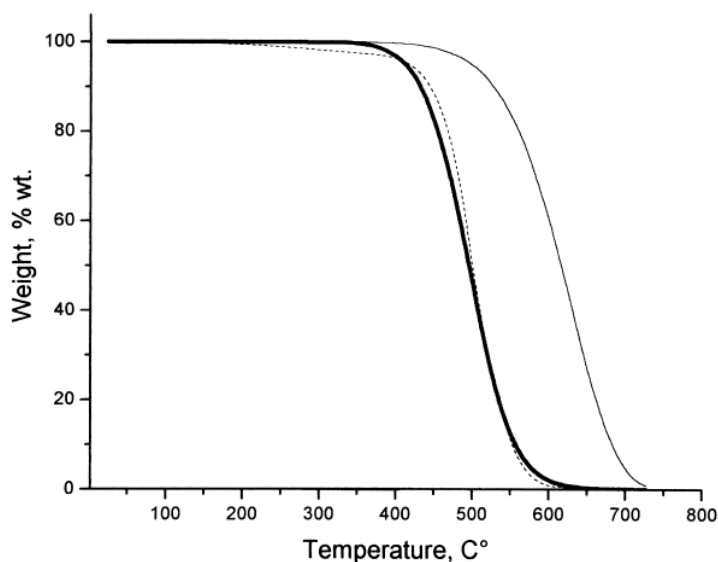


Figure 2.11 TGA thermograms of PDMS ( $N_2$ ,  $10^\circ Cmin^{-1}$ ) [62].

### 2.4.3 Applications of PDMS polymer

Due to the advantage of PDMS properties, PDMS is widely used in many applications including contact lens, medical device, sealants, optic device, antifoaming agent, and cosmetics [61]. Currently, it also uses as substrates to produce flexible conductive polymer [23, 29].



## CHAPTER III

### EXPERIMENTAL SECTION

#### 3.1 Chemical reagents

1. Granular silver metal (99.99% purity, 1-2 mm diameter, Gold Field Refinery Co. Ltd., Thailand)
2. Silver acetate crystal with columnar structure, commercially available grade; commercial columnar silver acetate CC-AcOAg (99% purity, Sigma Aldrich)
3. Ethyl acetate, AcOEt (Merck, Thailand)
4. Glacial acetic acid, AcOH (Merck, Thailand)
5. Hydrogen peroxide, H<sub>2</sub>O<sub>2</sub> (30% w/w) (Merck, Thailand)
6. Polydimethylsiloxane, SYLGARD® 184 (Dow Corning Corp., Midland, MI, USA)

#### 3.2 Instruments

1. Optical microscope, OM (Carl Zeiss Axio Scope. A1 with a CCD camera, Carl Zeiss, AxioCam HRc)
2. Scanning electron microscope, SEM (JEOL JSM-6510)
3. Fourier-transform infrared spectroscopy, FTIR (ATR, Thermo Scientific)
4. Raman microscope (DXR, Thermo Scientific)
5. Two-point probe multimeter (UNI-T, UT60G)
6. Thermal gravimetric analysis, TGA (Mettler-Toledo Ltd., Thailand)
7. Differential scanning calorimetry, DSC (Mettler-Toledo Ltd., Thailand)
8. X-ray diffractometer, XRD (Rigaku RINT2000)
9. Nitrogen adsorption-desorption analyzer (BEL Japan, Inc.)
10. 3D printer (SCOOVO C170, Japan)
11. Hotplate stirrer (Heidolph)
12. Furnace (RhinoTherm, Rojana, Thailand)
13. Sonicator (Elmasonic, E 30H)
14. Ultrasonicator (Sonics VCX-750 Vibra Cell)
15. Thermal evaporator (CRTM-6000G, ULVAC KIKO Inc., Japan)



### 3.3 Synthesis of rod-shaped silver acetate (RS-AcOAg)

Rod-shaped silver acetate (RS-AcOAg) was prepared as following: 82 mL of ethyl acetate (AcOEt), 6 mL of acetic acid (AcOH), and 12 mL of 30% w/w hydrogen peroxide ( $H_2O_2$ ) were mixed together. After that, the mixture was poured into a beaker, which contained 3 g of granular silver metal. The beaker was wrapped with aluminum foil for 48 hours at room temperature to allow the crystallization of AcOAg crystals as Bundle-AcOAg (Bun-AcOAg) which is compact packing of RS-AcOAg. After that, the Bun-AcOAg was purified by filtration and washed with AcOEt for several times until the filtrate reached pH 4.

To prepare RS-AcOAg, the filtrate of Bun-AcOAg from the previous step was dissolved in AcOEt and then, placed in an ultra-sonicator (Sonics VCX-750 Vibra Cell, power 250 watts) with 60% amplitude for 30 minutes.

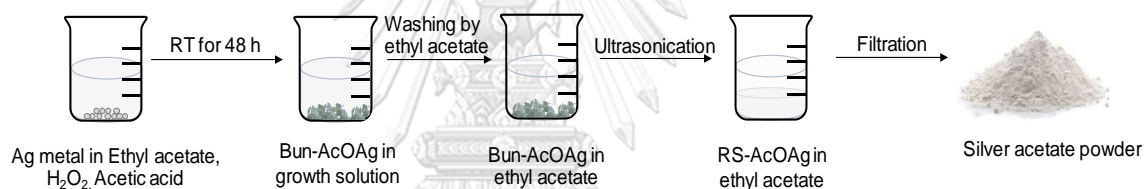


Figure 3.1 The schematic represented a step of rod-shaped RS-AcOAg synthesis.

### 3.4 Preparation of porous silver films with and without polydimethylsiloxane base (bPDMS) film coating

Silver acetate solution was prepared by disperse 0.3 g of the RS-AcOAg or commercial columnar (CC-AcOAg) in 3 ml of ethyl acetate. The mixtures were sonicated for 5 minutes and casted a film on the glass slide. The area of the film was  $1.5 \times 6.5 \text{ cm}^2$  which were limit the area by using polyimide (PI) tape. The films were further thermally decomposed at  $300^\circ\text{C}$  for 1 minute by using a furnace for convert into the porous silver films (Figures 3.2 (A1 and A2)). To study sintering effect, both RS-AcOAg and CC-AcOAg were coated with bPDMS. The mixtures were prepared by disperse 0.3 g of the RS-AcOAg in 3 mL of ethyl acetate. Then, a 0.003 g of bPDMS was added into the mixtures and sonicated for 5 minutes. The thin film was casted and decomposed as described above (Figures 3.2 (B1 and B2)).

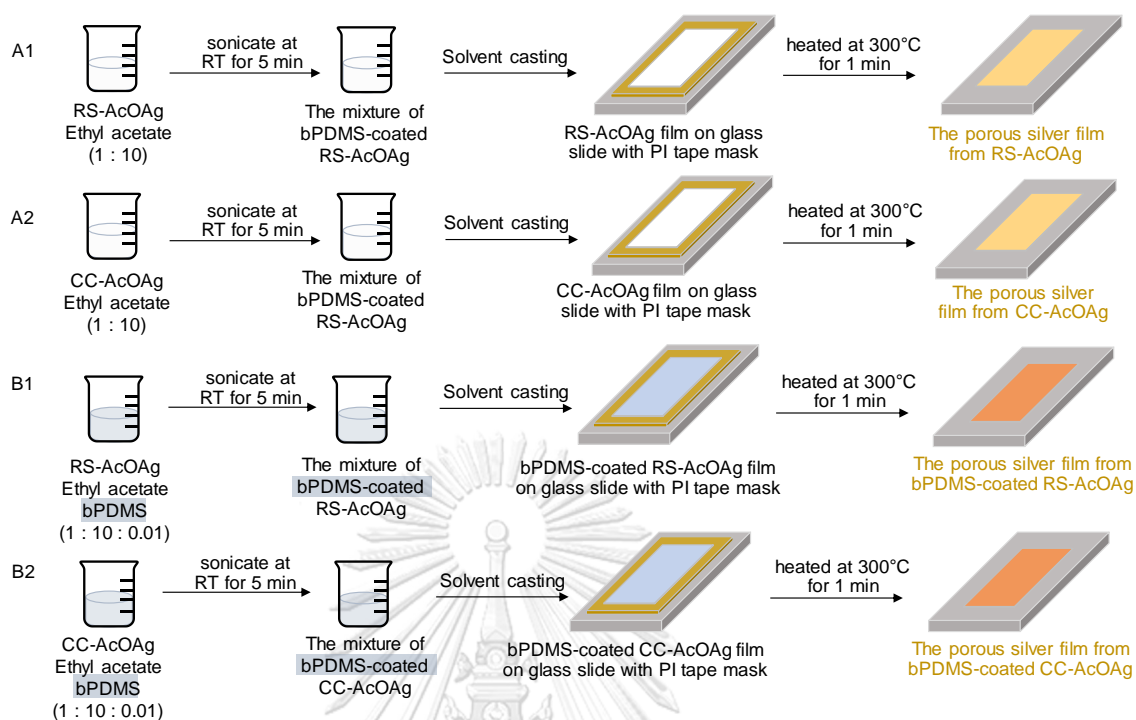


Figure 3.2 Schematic represented the preparation of a porous film by using (A1) RS-AcOAg, (A2) CC-AcOAg, (B1) bPDMS-coated RS-AcOAg, and (B2) bPDMS-coated CC-AcOAg.

### 3.5 Fabrication of porous silver films as flexible conductive strips

The porous silver films from thermally decomposed RS-AcOAg with and without bPDMS film coating were chosen to employ as raw materials for fabricating PDMS-silver composite as flexible conductive strips due to its thermal, morphological, and chemical composition properties.

PDMS substrate was prepared by mixing PDMS base with curing agent at 10:1 ratio. The mixture of PDMS was degassed by vacuum pump for an hour, then poured onto the porous silver films. After curing at 60°C for 3 hours, the cured-PDMS was cut into a strip and peel off from the glass slide to yield the porous silver conductive strip (Figure 3.3).

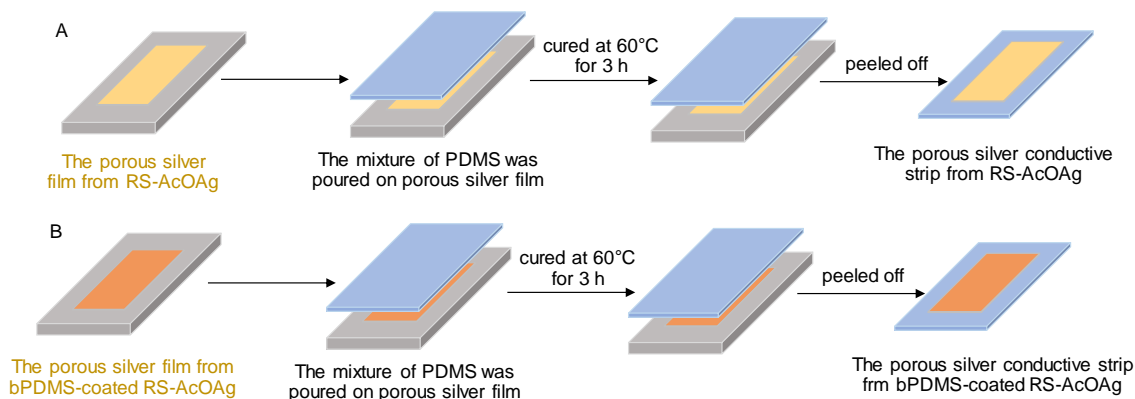


Figure 3.3 The fabrication of porous silver conductive strip from (A) RS-ACOAg and (B) bPDMS-coated RS-AcOAg.

### 3.6 Characterization the morphology of silver acetate and porous silver films

#### 3.6.1 Scanning Electron Microscopy (SEM)

Morphology and particles size of silver acetate samples: RS-AcOAc, bPDMS-coated RS-AcOAg, CC-AcOAg, and bPDMS-coated CC-AcOAg were observed by SEM with an accelerating voltage of 10 kV using secondary electron imaging (SEI) mode. A few milligrams of each silver acetate sample were dissolved in AcOEt. After that, the samples suspension was dropped and spread on a glass slide to form a silver acetate film. Then, the film was transferred onto the carbon tape which attached on an aluminum stub by stamping. To eliminate the remaining AcOEt, the samples were further evaporated for 10 minutes. The porous silver film of all samples was also prepared with the same protocol.

Energy-dispersive X-ray spectroscopy (EDS) mode of SEM with an accelerating voltage of 5kV, magnification of 3000X, and point analysis mode was used for identifying the elemental composition of the samples.

The length and width of the silver acetate samples and the silver particles size of the porous silver samples were determined by using ImageJ software ( $N = 300$ ).

### **3.6.2 Optical microscopy (OM)**

After porous silver conductive strips was fabricated, the morphology of porous structure was observed under conditions of no stretching, while stretching, and after stretching using refractive mode of optical microscope (OM) with a CCD camera and 100X objective lens.

## **3.7 Characterization of molecular information of the silver acetate before and after thermal decomposition**

### **3.7.1 Fourier-transform infrared spectroscopy**

The functional groups of RS-AcOAg and CC-AcOAg were investigated using iD7 ATR Fourier-transform infrared spectrometer (FT-IR), (Thermo Scientific). All FT-IR spectra were collected by attenuated total reflection (ATR) technique in a single reflection mode with a zinc selenide prism (Harrick, IRK-FTS). The spectral resolution was  $4\text{ cm}^{-1}$  and the number of scans was 64 in the spectral range of  $4000\text{-}700\text{ cm}^{-1}$ . Samples were prepared by placing a drop of samples solution on glass slide. After the sample solution was dried, spectrums were collected.

### **3.7.2 Raman spectroscopy**

Raman spectra of the silver acetate film was recorded by DXR Raman microscope with 532 nm excitation laser, 5-10 mW laser power, 32 numbers of scan, 25  $\mu\text{m}$  pinhole, and 20x objective lens were employed with a 1  $\mu\text{m}$  laser spot size. The silver acetate samples were prepared by dropping the silver acetate suspension on glass slide.

## **3.8 Characterization of diffraction pattern of silver acetate**

### **3.8.1 X-ray diffraction**

The RS-AcOAg and CC-AcOAg were dried at room temperature for 30 minutes by vacuum pump before characterizing XRD analysis. The XRD patterns were obtained with Rigaku RINT2000 X-ray diffractometer using Cu  $K\alpha_1$  radiation ( $\lambda = 0.154\text{ nm}$ ) and a power of 40 kV and 20 mA. The diffracted intensities were recorded at  $2\theta$  angles range from  $20^\circ$  to  $80^\circ$ .

### **3.9 Study of thermal properties of silver acetate and porous silver films**

#### **3.9.1 Thermal gravimetric analysis (TGA)**

The thermal decomposition profile of silver acetate was determined by using TGA measurements which performed by using a TGA instrument (Mettler-Toledo, Ltd., Thailand). The process was carried out under nitrogen gas flow at the rate of 50 cm<sup>3</sup>/min. The samples were prepared by placing a various amount of silver acetate samples with 5 mg on a ceramic pan. The samples were heated from 25°C to 900°C with the heating rate of 10°C/min.

#### **3.9.2 Differential Scanning Calorimetry (DSC)**

Crystallinity of the silver acetate samples (RS-AcOAc, bPDMS-coated RS-AcOAg, CC-AcOAg, and bPDMS-coated CC-AcOAg) were investigated by DSC measurements (Mettler-Toledo, Ltd., Thailand). All samples were placed into the DSC aluminum pans and heated from 25°C to 350°C with a heating rate of 10°C/min under nitrogen gas flow at the rate of 50 cm<sup>3</sup>/min. In this work, an empty pan was used as a reference.

#### **3.10 Study of surface area of porous silver films**

The surface area was determined by the Brunauer–Emmett–Teller (BET) method using nitrogen adsorption-desorption analyzer, BEL Japan, Inc. Belsorp mini II analyzer. The samples (approximately 5 mg) were prepared and degassed at room temperature for 30 minutes before the BET measurements. N<sub>2</sub> was used throughout the adsorption experiments. The BET surface areas were determined by using the data under the relative pressures between 0-1 before the capillary condensation. The pore size distributions were calculated from the adsorption data by the Barret–Joyner–Halenda (BJH) method.

#### **3.11 Electrical resistance measurement of porous silver conductive strip**

Three types of mechanical strain devices: stretching, bending, and twisting were fabricated by 3D printer (SCOOVO C170, Japan) and used for measuring an

electrical resistance by two-point probe multimeter (UNI-T, UT60G). For stretching test, the strip was fastened by the device, then, the strip was measured the electrical resistance while it was stretched. The changing length was measured by a ruler scale (Figure 3.4A). For bending and twisting test, the strip was also fastened by the device, then the strip was measured the electrical resistance while it was bended (Figure 3.4B) and twisted (Figure 3.4C). The degree of bending and twisting were measured by angle degree chart. The electrical resistance as mentioned before was measured with 2 types; 1) during continuously applied the mechanical force to the flexible conductive strip and 2) after 10 cycles of deformation of stretching, bending, and twisting.

To measure the electrical resistivity of the porous silver strips, the electrical resistivity was measured under the relative changes of the resistance ( $\Delta R/R_0$ ) where  $\Delta R/R_0 = (R-R_0)/R_0$ , where  $R_0$  is the electrical resistance of the strip before applied mechanical strain, and  $R$  is the resistance while applied the mechanical strain.



Figure 3.4 The mechanical strain devices (A) stretching, (B) bending, (C) twisting for electrical resistivity measurement.

## CHAPTER IV

### RESULTS AND DISCUSSION

#### 4.1 Synthesis of RS-AcOAg

Silver acetate (AcOAg) was prepared as follow: A homogenous mixture of 82 mL of ethyl acetate, 12 mL of hydrogen peroxide, 6 mL of acetic acid were prepared. Ethyl acetate acted as a solvent while hydrogen peroxide acted as an etchant for silver metal. Generally, the mixing of ethyl acetate and hydrogen peroxide were not the homogeneous mixture. When an acetic acid was added into the mixture, it turned into the homogeneous mixture. Acetic acid acted as an emulsifier. Then, the homogeneous mixture was poured into a beaker, which contained 3 g of silver metal. The beaker was covered with food wrap for 48 hours at room temperature to allow the formation of the flower-shaped silver acetate (FS-AcOAg), then, FS-AcOAg fell off and became bundle silver acetate (Bun-AcOAg) (Figure 4.1).

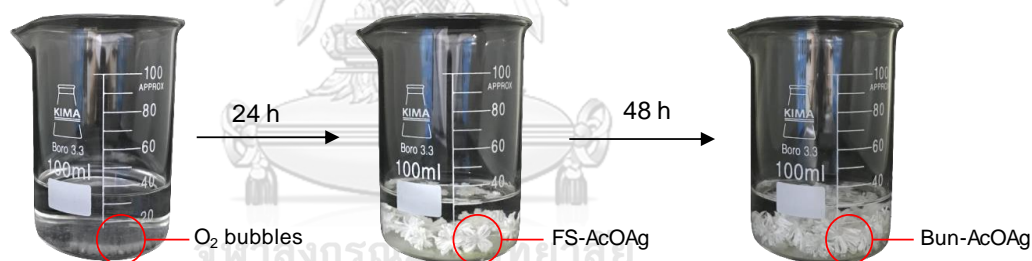
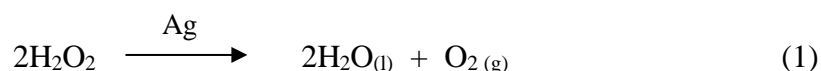


Figure 4.1 Digital photographs showing crystal growth of AcOAg.

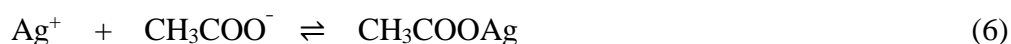
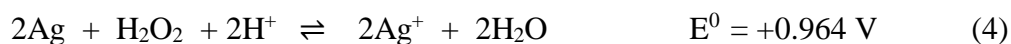
While the reaction was proceeding, bubbles of O<sub>2</sub> gas were generated in the solution via the catalytic decomposition of hydrogen peroxide over silver metals (Eq.1). Normally, hydrogen peroxide is thermodynamically unstable and slowly decomposed into water and O<sub>2</sub> gas without a formation of O<sub>2</sub> gas bubbles [63].



Silver metals were oxidized by hydrogen peroxide to form silver ions (Ag<sup>+</sup>), the silver ions were released into the solution (Eq.4) while an acetic acid was



dissociated into acetate ions ( $\text{CH}_3\text{COO}^-$ ) (Eq.5). Subsequently, silver ions reacted with acetate ions and formed AcOAg crystals (Eq.6).



The reaction mixture was left undisturbed for 24 hours, allowing a formation of flower-shaped silver acetate (FS-AcOAg). After that, the petals of FS-AcOAg tended to fall off due to complete dissolution of silver metal and bundled silver acetate structures (Bun-AcOAg) were formed. Bun-AcOAg consists of densely packed rod-shaped silver acetate (RS-AcOAg) (Figure 4.2).



Figure 4.2 The morphological growth of AcOAg crystals.

#### 4.2 Morphology of RS-AcOAg

Bun-AcOAg was obtained as the final product from the AcOAg preparation (Figure 4.2). However, rod-shaped RS-AcOAg was required to use as conductive materials in this work. Therefore, RS-AcOAg had to be disassembled from Bun-AcOAg by the ultra-sonication technique.

The morphological details of RS-AcOAg were observed by scanning electron microscope. Bun-AcOAg petals (Figure 4.3A1) was a dense packing of RS-AcOAg (Figure 4.3A2). After an ultra-sonication with an ultrasonic probe operated at 750 kW with frequency of 20 kHz and 60% amplitude, Bun-AcOAg was disintegrated into RS-AcOAg (Figure 4.3B1). RS-AcOAg possessed the distribution of Bun-AcOAg after ultra-sonication (Figure 4.3B2).



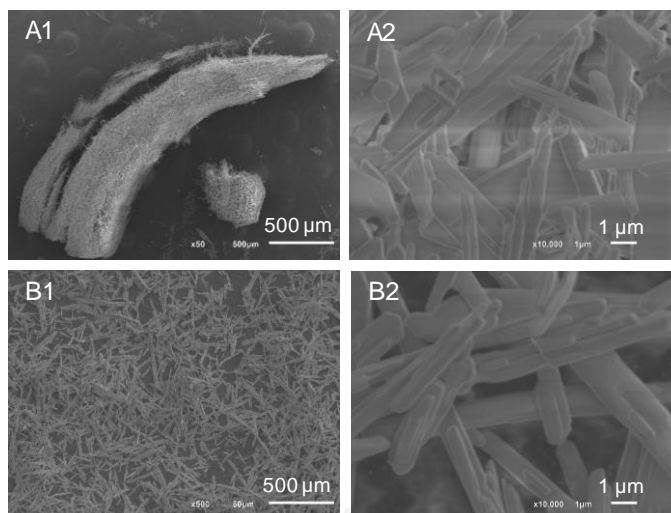


Figure 4.3 SEM micrographs of (A) Bun-AcOAg and (B) RS-AcOAg.

### 4.3 Comparison between RS-AcOAg and CC-AcOAg

#### 4.3.1 Dimensions

RS-AcOAg and CC-AcOAg were sonicated in ethyl acetate before measurement. The obtained slurry was dropped on an aluminum stub for morphological characterization with a scanning electron microscope (SEM). The widths and lengths of RS-AcOAg and CC-AcOAg were measured directly from SEM micrographs. Dimension of RS-AcOAg and CC-AcOAg were measured from 300 particles using ImageJ program. The size distribution histograms of RS-AcOAg and CC-AcOAg were compared.

The average width and length of RS-AcOAg (Figure 4.4) were  $1.4 \pm 0.4 \mu\text{m}$  and  $14.0 \pm 5.0 \mu\text{m}$ , respectively. In contrast, the average width and length of CC-AcOAg (Figure 4.4) were  $4.9 \pm 1.0 \mu\text{m}$  and  $38 \pm 15 \mu\text{m}$ , respectively. RS-AcOAg were 3-times smaller than CC-AcOAg in both width and length. In addition, the distribution in the dimensions of RS-AcOAg were less than those of CC-AcOAg. As reported by Yilan Ye (2018), the aspect ratio (the ratio of length to width) of rod-shaped structure was between 2 to 24 [64]. Herein, the aspect ratio values of RS-AcOAg and CC-AcOAg were 10 and 8, respectively. The aspect ratio of RS-AcOAg was 23% greater than that of CC-AcOAg. The high aspect ratio of conductive materials might enhance the electrical conductivity of flexible conductive strips [65].

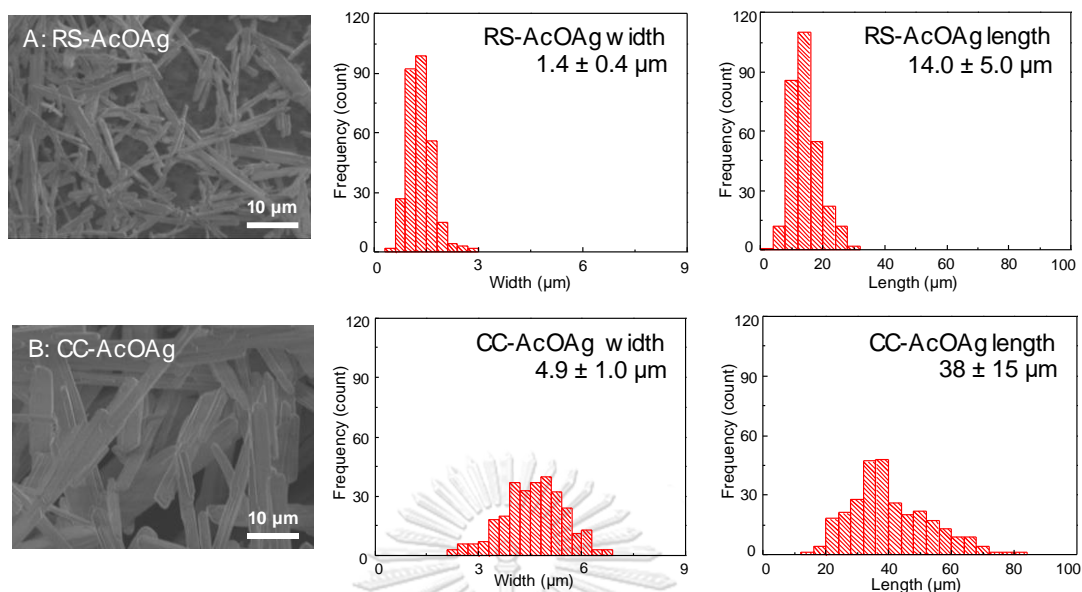


Figure 4.4 SEM micrographs of (A) RS-AcOAg and (B) CC-AcOAg and the corresponding size distribution of widths and lengths.

### 4.3.2 Molecular information

To confirm that RS-AcOAg and CC-AcOAg are the same materials, Fourier-transform infrared spectroscopy (FTIR), Raman spectroscopy, and X-ray powder diffraction (XRD) techniques were used for characterization. FTIR spectra of RS-AcOAg and CC-AcOAg (Figure 4.5A) show the same characteristic peaks of AcOAg as asymmetric C-O stretching ( $1592\text{ cm}^{-1}$ ), symmetric C-O stretching ( $1420\text{ cm}^{-1}$ ), symmetric  $\text{CH}_3$  deformation ( $1350\text{ cm}^{-1}$ ), in plane  $\text{CH}_3$  rocking ( $1020\text{ cm}^{-1}$ ), C-C stretching ( $930\text{ cm}^{-1}$ ), O-C-O bending ( $660\text{ cm}^{-1}$ ), and out of plane O-C-O ( $620\text{ cm}^{-1}$ ) [66]. In addition, Raman spectra of RS-AcOAg and CC-AcOAg (Figure 4.5B) also show the same characteristic peaks of AcOAg as C-H stretching ( $3009\text{ cm}^{-1}$ ,  $2940\text{ cm}^{-1}$ ), symmetric C-H bending ( $1414\text{ cm}^{-1}$ ), symmetric O-C-O stretching ( $1347\text{ cm}^{-1}$ ), and symmetric C- $\text{CH}_3$  in plane bending ( $934\text{ cm}^{-1}$ ) [67]. XRD patterns of RS-AcOAg and CC-AcOAg (Figure 4.5C) show the same characteristic peaks that the unit cell for AcOAg was determined to be triclinic [45].

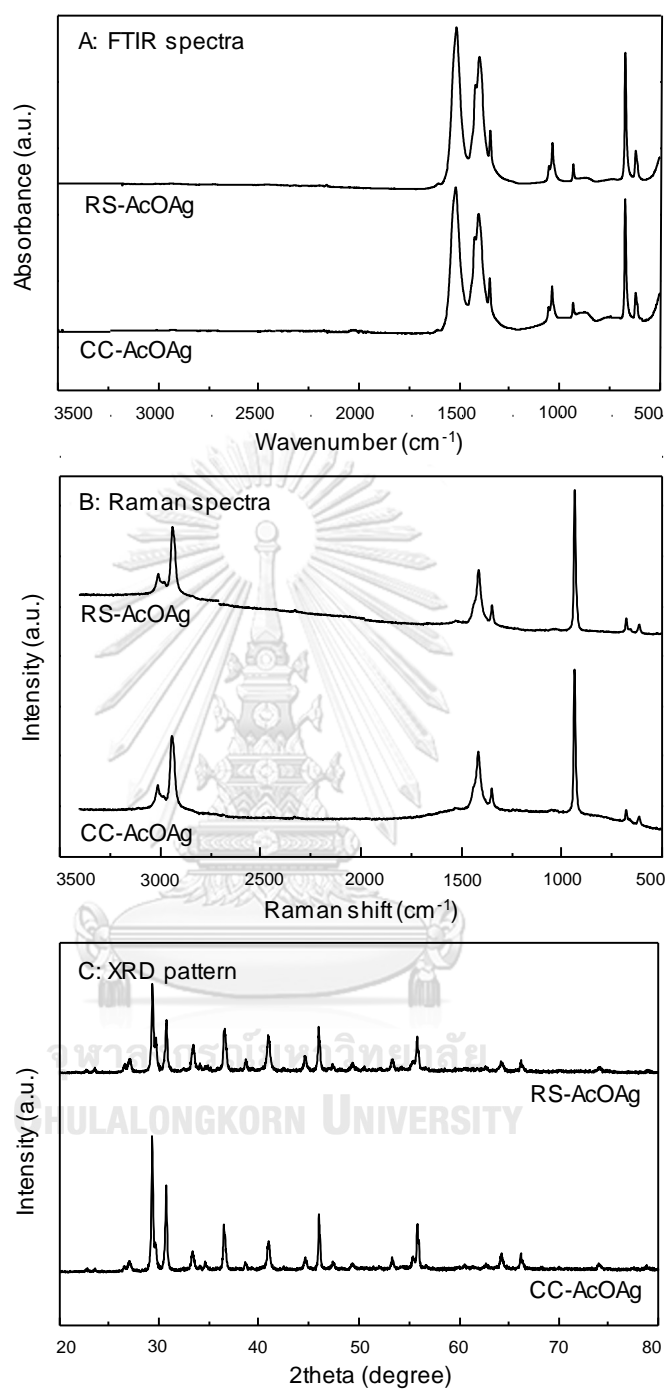


Figure 4.5 (A) FTIR spectra, (B) Raman spectra, and (C) XRD patterns of RS-AcOAg and CC-AcOAg.

### 4.3.3 Thermal decomposition

In order to utilize RS-AcOAg and CC-AcOAg as conductive materials for fabricating PDMS-silver flexible conductive strips, they must be thermally decomposed to silver metal. Thermogravimetric analysis (TGA) and differential scanning calorimetry (DSC) were employed for investigating the thermal decomposition of RS-AcOAg and CC-AcOAg. Thermal decomposition of AcOAg as  $\text{CH}_3\text{COOAg}$  under nitrogen atmosphere is shown in Eq.7 [45].



The thermogravimetric (TG) and the corresponding differential thermogravimetric (DTG) thermograms of RS-AcOAg and CC-AcOAg are shown in Figure 4.6.

The TG thermograms show the onset temperatures, which are the temperature where weight loss begins, of RS-AcOAg and CC-AcOAg at 268°C and 276°C, respectively (Figure 4.6). The lower onset temperature of RS-AcOAg suggested that the thermal decomposition of RS-AcOAg was initiated at a lower temperature than that of CC-AcOAg due to the better thermal transfer of small particles. The smaller sizes of RS-AcOAg increase surface area, causing an improvement in the thermal absorption ability [68]. The derivative TG thermograms showed decomposition temperature of RS-AcOAg and CC-AcOAg at 287°C and 284°C, respectively. The insignificant differences in the thermal decomposition profiles of RS-AcOAg and CC-AcOAg implied that RS-AcOAg and CC-AcOAg possessed the same thermal decomposition properties (Figure 4.6).

The weight loss values at 400°C of RS-AcOAg and CC-AcOAg were approximately at 35.0% and 35.4%, respectively (Table 4.1). The weight loss referred to the decomposition of organic part of AcOAg as acetate group [49]. The residual weights at 400°C of RS-AcOAg and CC-AcOAg were 65.0% and 64.6%, respectively (Table 4.1). The residual weight at 400°C was attributed to silver and carbon residue, according to Eq.7 [45]. The weight loss values and the residual weights of RS-AcOAg and CC-AcOAg were approximately the same as the theoretical values of 32.8% and 68.2%, respectively.

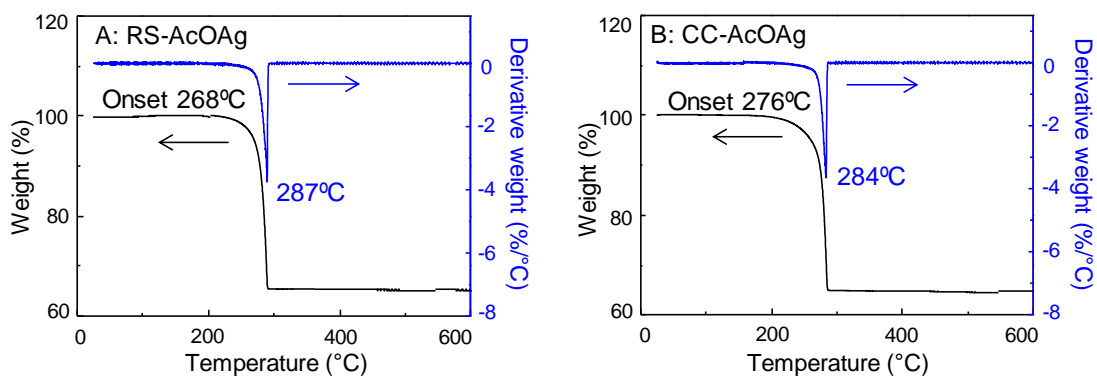


Figure 4.6 TG and the corresponding DTG curves of (A) RS-AcOAg and (B) CC-AcOAg.

Table 4.1 Thermal properties of RS-AcOAg and CC-AcOAg.

Materials	Onset temperature (°C)	Decomposition temperature (°C)	Residual weight at 400°C (%)	Weight loss at 400°C (%)
RS-AcOAg	268	287	65.0	35.0
CC-AcOAg	276	284	64.6	35.4

The DSC profiles of RS-AcOAg and CC-AcOAg within the range of 25°C to 350°C exhibited a single exothermic peak (Figure 4.7). The exothermic peak temperatures of RS-AcOAg and CC-AcOAg were 282°C and 288°C, respectively. The exothermic peak temperature was assigned to the decomposition reaction of AcOAg into silver metal [48]. The exothermic temperatures of RS-AcOAg and CC-AcOAg were slightly different (6°C) as a result of the different sizes of RS-AcOAg and CC-AcOAg. The smaller sizes of RS-AcOAg increase surface area, causing an improvement in the thermal absorption ability [68] and lowering decomposition temperature. The enthalpies of the reactions ( $\Delta H$ ) determined from the area under the exothermic peaks of RS-AcOAg and CC-AcOAg were 63.75 Jg<sup>-1</sup> and 67.18 Jg<sup>-1</sup>, respectively. The thermal decomposition of both RS-AcOAg and CC-AcOAg are exothermic due to the decomposition of acetic acid residue as the AcOAg was decomposing [48].

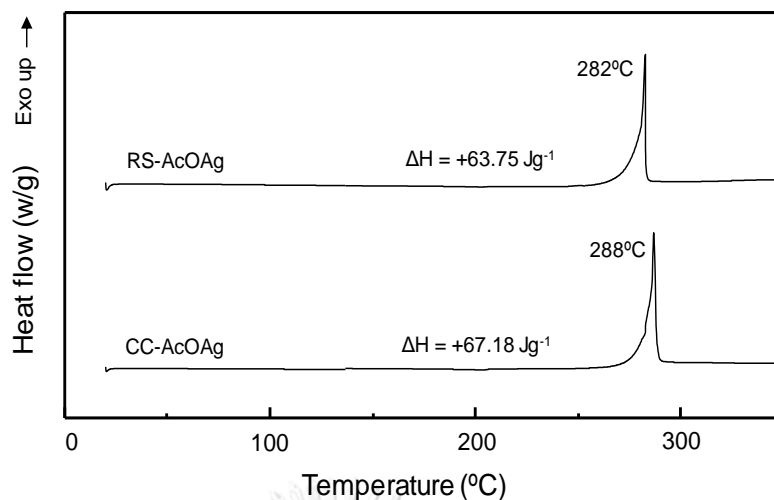


Figure 4.7 DSC thermograms of RS-AcOAg and CC-AcOAg.

#### 4.3.4 Thermal dependence decomposition and sintered structures

Thermal decomposition of RS-AcOAg and CC-AcOAg were studied at RT, 200°C, 250°C, and 300°C. RS-AcOAg and CC-AcOAg must be thermally decomposed to form silver metal as porous silver structures which was used for being conductive materials. While RS-AcOAg and CC-AcOAg were thermally decomposing, the porous silver structures became sintered structures due to fusing of silver particles during heating.

Sintering is the process of compacting and forming contacts between particles during heating. Atoms in the materials diffuse across the boundaries of the particles, fusing the particles together and creating the rigid structure [53].

The morphological profiles and silver particles growth of RS-AcOAg and CC-AcOAg were investigated by a scanning electron microscope (SEM) with thermal dependence decomposition at RT, 200°C, 250°C, and 300°C. At room temperature, the shape of RS-AcOAg and CC-AcOAg were rod shape with the width of  $1.4 \pm 0.4 \mu\text{m}$  (Figures 4.8A1) and columnar shape with the width of  $4.9 \pm 1.0 \mu\text{m}$  (Figure 4.8B1), respectively. When the temperature was raised to 200°C,  $0.1 \pm 0.02 \mu\text{m}$  silver nanoparticles (AgNPs) were formed and presented as small particles on RS-AcOAg surfaces (Figure 4.8A2). On the other hand,  $0.18 \pm 0.06 \mu\text{m}$  AgNPs were partially formed on edges of CC-AcOAg (Figure 4.8B2). After the temperature increased to 250°C, AgNPs with quasi-spherical shape of both RS-AcOAg and CC-AcOAg were

fused together to form bigger particles as silver microparticles (AgMPs) with  $0.25\pm 0.07\ \mu\text{m}$  and  $0.73\pm 0.22\ \mu\text{m}$ , respectively (Figures 4.8 (A3 and B3)). Finally, when the temperature was raised to  $300^\circ\text{C}$ , each melted AgMPs chains of both RS-AcOAg and CC-AcOAg were became extensively sintered porous silver structures with size of AgMPs as  $0.95\pm 0.16\ \mu\text{m}$  and  $2.3\pm 0.46\ \mu\text{m}$ , respectively (Figures 4.8 (A4 and B4)).



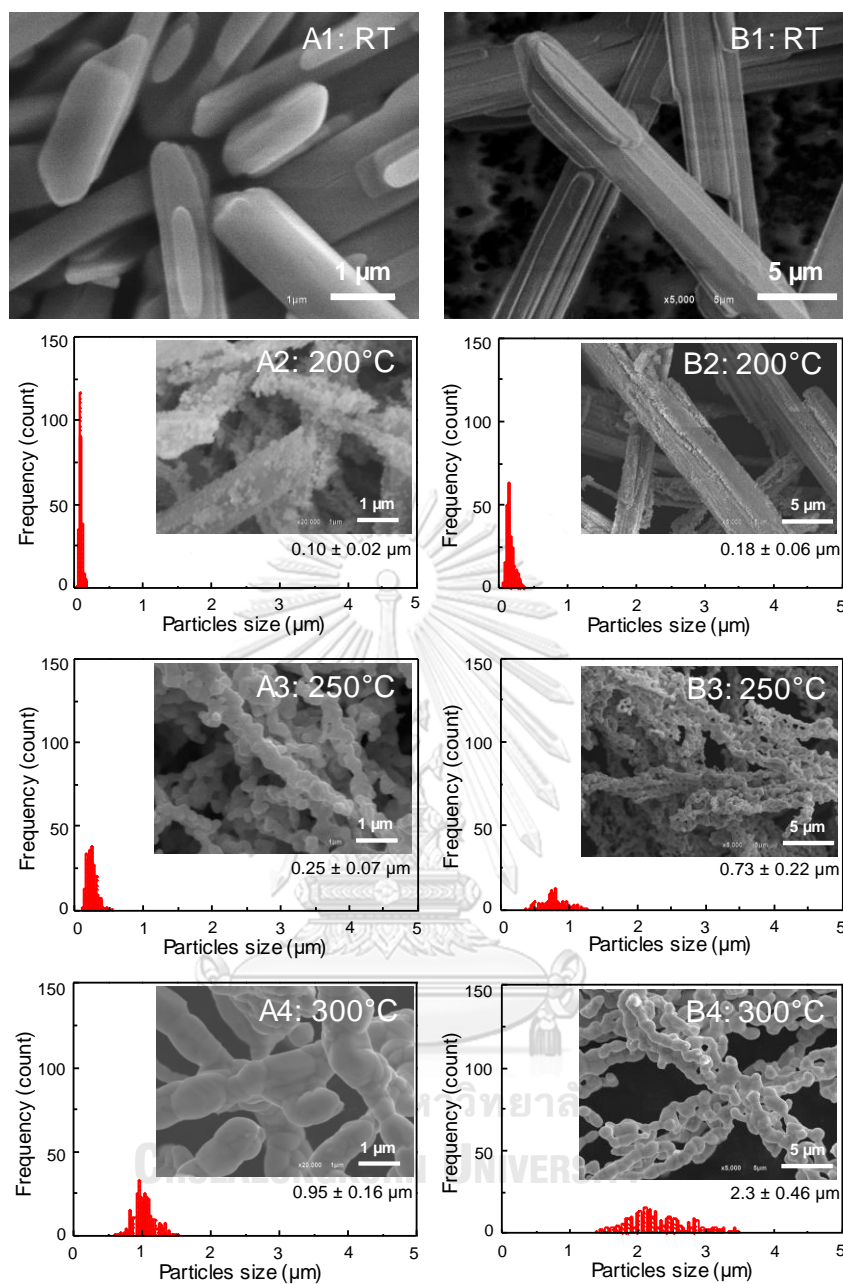


Figure 4.8 Size distribution of AgMPs obtained by decomposition of (A) RS-AcOAg and (B) CC-AcOAg at 200°C, 250°C, and 300°C.

To study the molecular information of RS-AcOAg and CC-AcOAg at various temperature of RT, 200°C, 250°C, and 300°C, FTIR technique was used. FTIR spectra of RS-AcOAg and CC-AcOAg at RT show the same characteristic peaks as asymmetric C-O stretching ( $1592\text{ cm}^{-1}$ ), symmetric C-O stretching ( $1420\text{ cm}^{-1}$ ), symmetric  $\text{CH}_3$  deformation ( $1350\text{ cm}^{-1}$ ), in plane  $\text{CH}_3$  rocking ( $1020\text{ cm}^{-1}$ ), C-C



stretching ( $930\text{ cm}^{-1}$ ), O-C-O bending ( $660\text{ cm}^{-1}$ ), and out of plane O-C-O ( $620\text{ cm}^{-1}$ ) (Figures 4.9 (A and B)). When the temperature was raised up to  $200^\circ\text{C}$  and  $250^\circ\text{C}$ , both RS-AcOAg and CC-AcOAg are remain the same characteristic peaks, thus, RS-AcOAg and CC-AcOAg were not completely decomposed and the AcOAg remained at those temperatures. However, when the decomposition temperature was increased to  $300^\circ\text{C}$ , the characteristic peaks of RS-AcOAg and CC-AcOAg were disappeared due to a complete decomposition of AcOAg. This means both RS-AcOAg and CC-AcOAg were completely decomposed into silver metal.

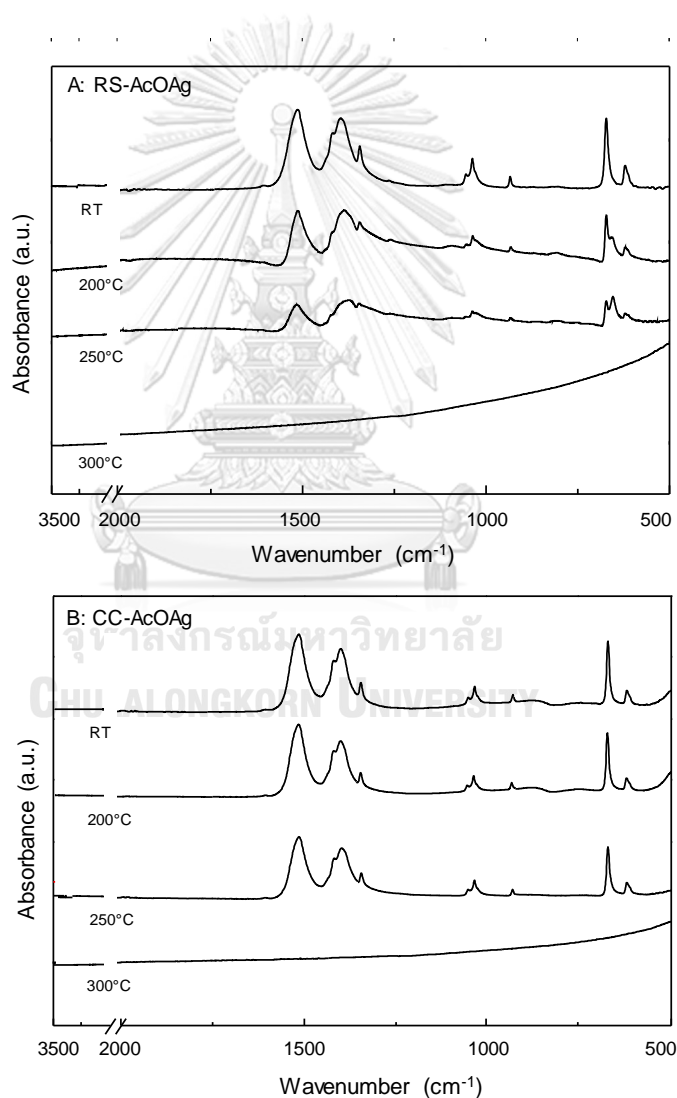


Figure 4.9 FTIR spectra of thermally decomposed (A) RS-AcOAg and (B) CC-AcOAg at RT,  $200^\circ\text{C}$ ,  $250^\circ\text{C}$ , and  $300^\circ\text{C}$ .

#### 4.3.5 Suppressed sintering porous silver structure by bPDMS

Extensively sintered structures of RS-AcOAg and CC-AcOAg after thermal decomposition at 300°C made the porous silver structure rigid due to the necking and fusing of neighboring AgMPs [56-57]. The extensively sintered structures tended to crack when the mechanical forces were applied [36]. To suppress extensive sintering, small amount of polydimethylsiloxane base (bPDMS) was used as a film coated onto the surface of RS-AcOAg and CC-AcOAg. The bPDMS possessed good thermal stability, good chemical resistance, and inertness [61]. Moreover, bPDMS can dissolve in ethyl acetate, which is used as solvent [69].

Thermal stability of bPDMS was investigated by thermogravimetric analysis. The thermogravimetric (TG) thermogram was shown in Figure 4.10. The onset temperature of weight loss at 389°C determined by TGA analysis, suggested that bPDMS was thermally stable at the temperature being investigated. It remained in the porous silver structure for suppressing sintered structure when the AcOAg was thermally decomposed at 300°C.

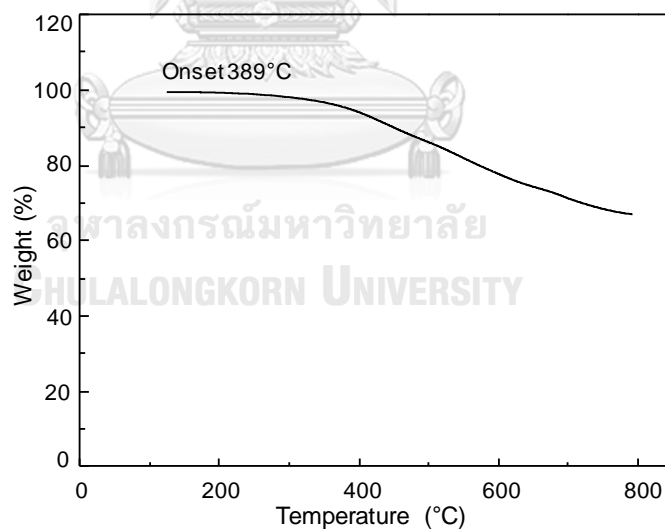


Figure 4.10 TG thermogram of bPDMS.

To suppress sintering, small amount of polydimethylsiloxane base (bPDMS) was used as a thin film coating onto the surface of RS-AcOAg.

In order to determine optimum amount of bPDMS for thermal decomposition of RS-AcOAg, (bPDMS-free, 0.001 g, 0.003 g, 0.005 g, 0.01 g, and 0.02 g) was

mixed with 10% wt/wt of RS-AcOAg in ethyl acetate (0.3 g of RS-AcOAg and 3.0 g of ethyl acetate). Then, the mixture was solvent casted on a glass slide to fabricate bPDMS-coated RS-AcOAg film. The film was dried in vacuum chamber at room temperature and was thermally decomposed at 300°C. After thermal decomposition, the color of all samples changed from white to dark yellow, depending on the amount of bPDMS (Figure 4.11).

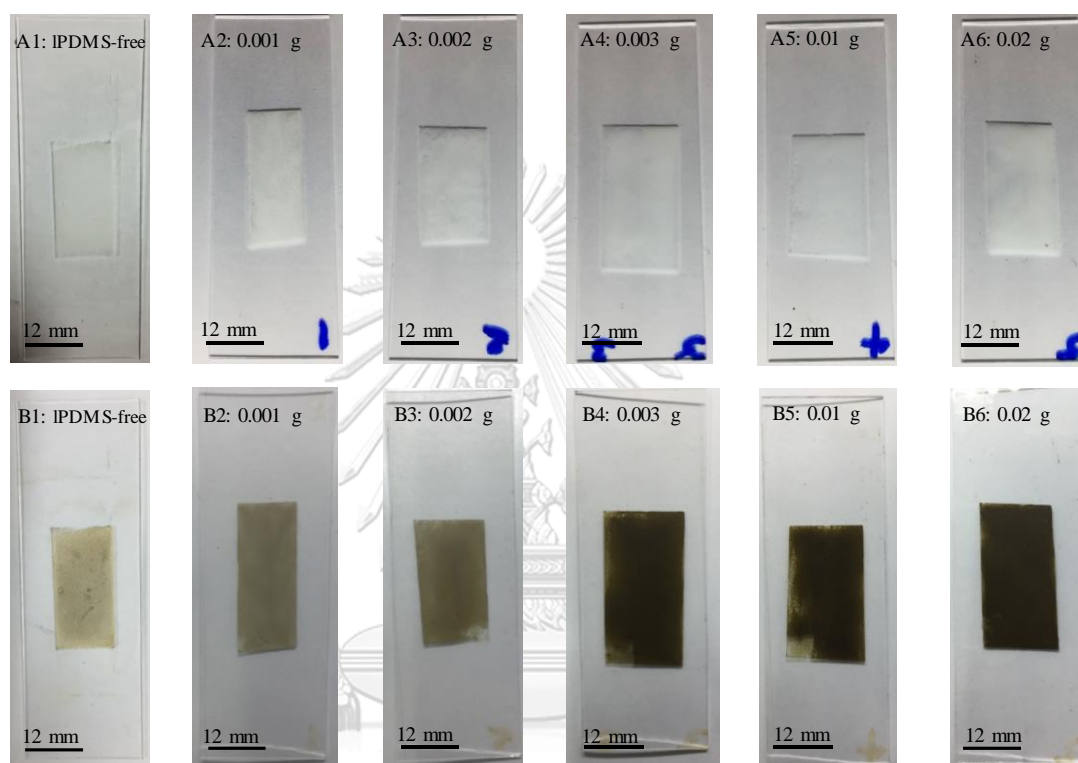


Figure 4.11 Photographic images of (A) bPDMS-coated RS-AcOAg on glass substrates at room temperature and (B) thermally decomposed at 300°C at various amount of bPDMS: (1) bPDMS-free, (2) 0.001 g, (3) 0.003 g, (4) 0.005 g, (5) 0.01 g, and (6) 0.02 g.

Figure 4.12 presented SEM micrographs of bPDMS-free RS-AcOAg and bPDMS-coated RS-AcOAg films before and after thermal decomposition. When the amount of bPDMS was lower than 0.01 g (Figures 4.12 (A1-A5)), RS-AcOAg was uniformly coated with bPDMS. However, bPDMS was formed as a continuous fluid film when the amount of PDMS was more than 0.01 g (Figure 4.12A6). After thermal decomposition, bPDMS-free RS-AcOAg and bPDMS-coated RS-AcOAg were transformed to porous silver structure. When the amount of bPDMS was 0.001 g

(Figure 4.12B2), the porous silver structure remained the sintering of silver particles as compared to structure that obtained from thermal decomposition of bPDMS-free RS-AcOAg (Figure 4.12B1). When the amount of bPDMS was added up to 0.003 g, sintering was suppressed, and the rod shape of porous silver structures were formed (Figure 4.12B3). However, when the bPDMS was more than 0.005 g (Figures 4.12 (B4-B6)), silver particles could be mobilized into fluid bPDMS and the porous structures were deformed.

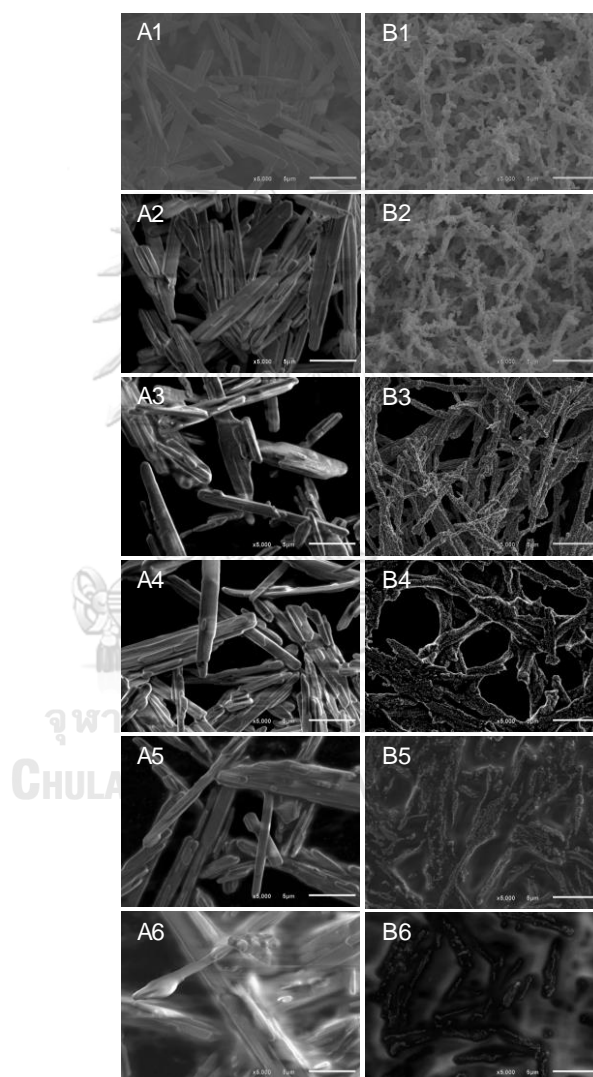


Figure 4.12 SEM micrographs of (A) bPDMS-coated RS-AcOAg films on glass substrates at room temperature and (B) the corresponding thermally decomposed films at 300°C with various amount of bPDMS: (1) bPDMS-free, (2) 0.001 g, (3) 0.003 g, (4) 0.005 g, (5) 0.01 g, and (6) 0.02 g.

When an excess bPDMS was added into RS-AcOAg, the mixture tended to be a liquid form. When the mixture was casted to form bPDMS-coated RS-AcOAg film and the film was thermally decomposed to porous silver structure (Figure 4.13A1), the silver particles might be released into the mixture (Figure 4.13A2). To confirm the migration of silver particles into bPDMS, the coated bPDMS was dissolved by rinsing the film with ethyl acetate and the remained silver structures were observed with a SEM. The remained structures after dissolving bPDMS were not porous structures and were deformed due the mobilization of silver particles into ethyl acetate (Figure 4.13B1). In addition, the color of ethyl acetate after the bPDMS dissolution was yellow, indicating the dissolution of dispersed silver nanoparticles. These results confirmed that an excessive amount of bPDMS affected the deformation of AcOAg structure after the thermal decomposition (Figure 4.13B2).

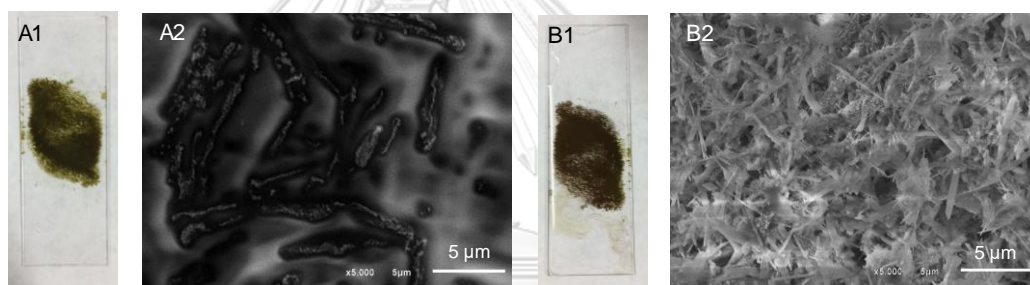


Figure 4.13 Digital photographs and the corresponding SEM micrographs of (A) porous silver from excess bPDMS-coated RS-AcOAg, and (B) A after rinsing by ethyl acetate.

From previous investigation, 0.003 g of bPDMS was selected as the optimum amount for RS-AcOAg film casting due to the effective suppression of silver particle sintering and preservation of porous silver structure after thermal decomposition (Figure 4.12B2), which was appropriate for fabricating flexible conductive strips.

## 4.4 Comparison of RS-AcOAg and CC-AcOAg after coating with bPDMS

### 4.4.1 Thermal decomposition

RS-AcOAg and CC-AcOAg were coated with the optimum amount of bPDMS to suppress sintering. Thermal decomposition profiles of RS-AcOAg, bPDMS-coated RS-AcOAg, CC-AcOAg, and bPDMS-coated CC-AcOAg were investigated and compared. The differential thermogravimetric (DTG) thermograms and thermogravimetric (TG) profiles of all samples are shown in Figure 4.14 and Figure 4.15, respectively.

TG thermograms showed the onset temperatures of the samples. The onset temperatures of RS-AcOAg and bPDMS-coated RS-AcOAg were 268°C and 269°C, respectively (Figures 4.14 (A1 and A2)). The onset temperatures of CC-AcOAg, and bPDMS-coated CC-AcOAg were 276°C and 275°C, respectively (Figures 4.14 (B1 and B2)). As obviously shown, the onset temperatures of them are insignificant difference with or without being coated with bPDMS. DTG thermograms showed single maximum thermal decomposition temperatures for all samples (Figure 4.13). The thermal decomposition temperatures of bPDMS-coated RS-AcOAg and bPDMS-coated CC-AcOAg slightly decreased compare to those of RS-AcOAg and CC-AcOAg because the thermal conductivity of bPDMS film which was coated onto the surface of AcOAg is higher than that of nitrogen gas for 100 times [70], thus, the bPDMS induced the decomposition of AcOAg more quickly so the decomposition temperatures of bPDMS-coated RS-AcOAg and bPDMS-coated CC-AcOAg decreased.

TG thermograms of RS-AcOAg, bPDMS-coated RS-AcOAg, CC-AcOAg, and bPDMS-coated CC-AcOAg (Figure 4.15) showed that the thermal stability of bPDMS-coated RS-AcOAg and bPDMS-coated CC-AcOAg slightly decreased when they were film coated by bPDMS, according to the thermal conductivity effect of bPDMS.

The weight loss values at 400°C of RS-AcOAg, bPDMS-coated RS-AcOAg, CC-AcOAg, and bPDMS-coated CC-AcOAg were 35.0%, 35.8%, 35.4%, and 35.7%, respectively (Table 4.2). The residual weights at 400°C of RS-AcOAg, bPDMS-coated RS-AcOAg, CC-AcOAg, and bPDMS-coated CC-AcOAg were 65.0%, 64.2%,

64.6%, and 64.3%, respectively (Table 4.2). The weight loss values and residual weights at 400°C of all samples were also approximately the same as the theoretical values of 35.4% and 64.6% respectively [49] (Table 4.2).

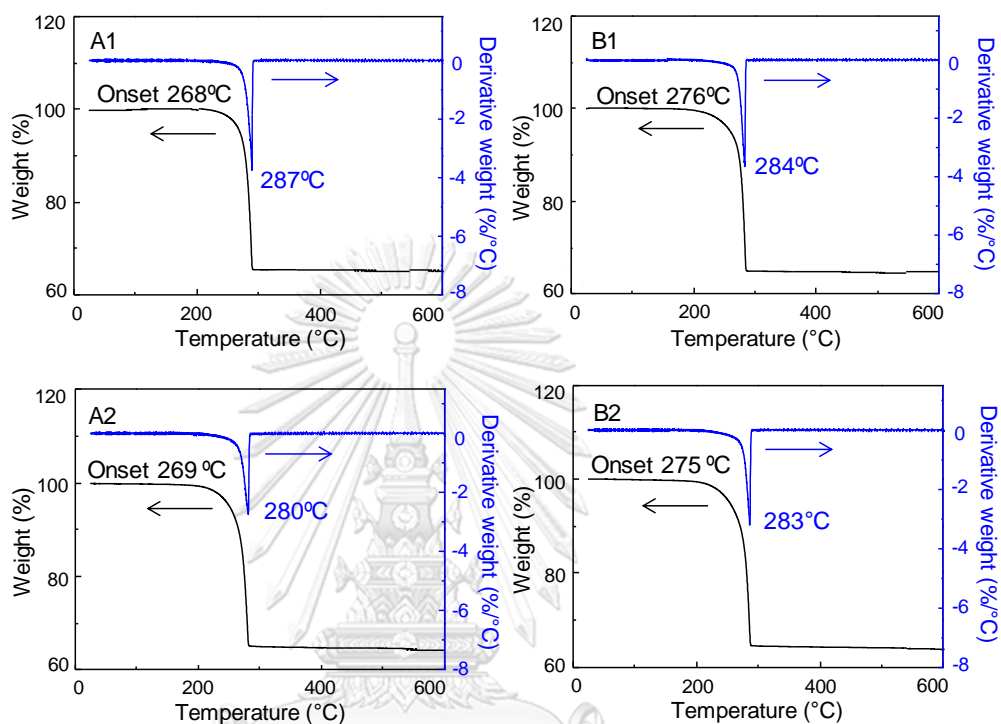


Figure 4.14 TG thermograms and the corresponding DTG thermograms of (A1) RS-AcOAg, (A2) bPDMS-coated RS-AcOAg, (B1) CC-AcOAg, and (B2) bPDMS-coated CC-AcOAg.

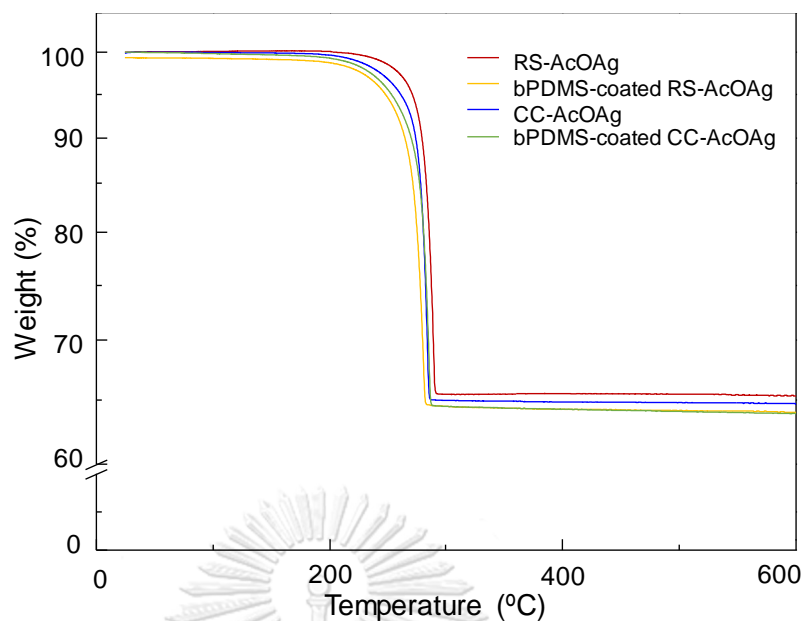


Figure 4.15 TG thermograms of RS-AcOAg, bPDMS-coated RS-AcOAg, CC-AcOAg, and bPDMS-coated CC-AcOAg.

Table 4.2 Thermal properties of RS-AcOAg, bPDMS-coated RS-AcOAg, CC-AcOAg, and bPDMS-coated CC-AcOAg.

Materials	Onset temperature (°C)	Decomposition temperature (°C)	Residual weight at 400°C (%)	Weight loss at 400°C (%)
RS-AcOAg	268	287	65.0	35.0
bPDMS-coated RS-AcOAg	269	280	64.2	35.8
CC-AcOAg	276	284	64.6	35.4
bPDMS-coated CC-AcOAg	275	283	64.3	35.7



DSC profiles of all samples were scanned from 25°C to 350°C. The exothermic peak temperatures of RS-AcOAg, bPDMS-coated RS-AcOAg, CC-AcOAg, and bPDMS-coated CC-AcOAg were 282, 286, 288, and 291°C, respectively (Figure 4.16). As mention before, the thermal decomposition of all samples is exothermic reaction due to the decomposition of acetic acid residue releasing by the decomposition of AcOAg [48]. When RS-AcOAg and CC-AcOAg were coated with bPDMS, the exothermic temperatures of bPDMS-coated RS-AcOAg and bPDMS-coated CC-AcOAg are insignificant difference, whereas the corresponding enthalpy changes ( $\Delta H$ ) decreased. The enthalpies of decomposition reaction of RS-AcOAg, bPDMS-coated RS-AcOAg, CC-AcOAg, and bPDMS-coated CC-AcOAg are 63.75 Jg<sup>-1</sup>, 47.38 Jg<sup>-1</sup>, 67.18 Jg<sup>-1</sup>, and 46.44 Jg<sup>-1</sup>, respectively. The enthalpy changes of bPDMS-coated RS-AcOAg and bPDMS-coated CC-AcOAg significantly decreased when compared to those of RS-AcOAg and CC-AcOAg. The bPDMS could absorb some acetic acid residue [71] while bPDMS-coated RS-AcOAg and bPDMS-coated CC-AcOAg were thermally decomposed. The adsorbed acetic acid residue is not be decomposed, resulting in the reduction of exothermic enthalpy.

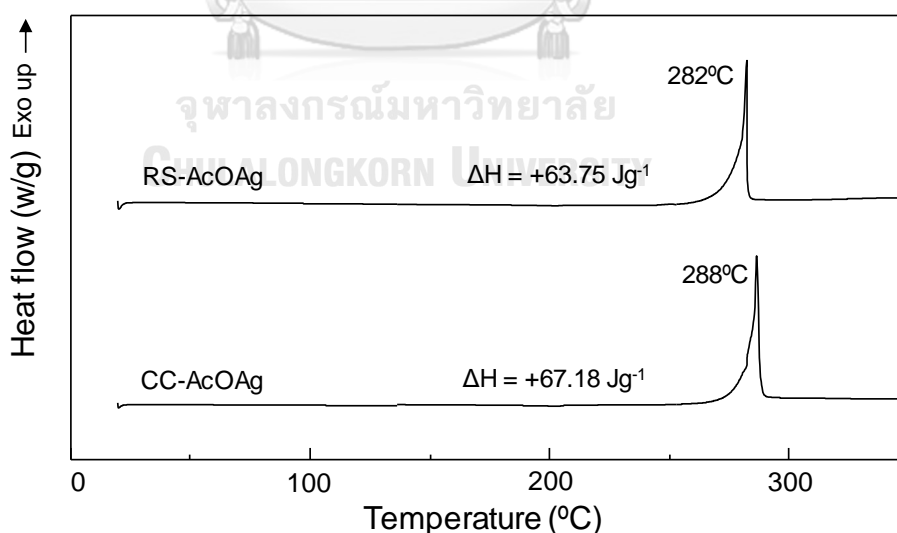


Figure 4.16 DSC profiles of RS-AcOAg, bPDMS-coated RS-AcOAg, CC-AcOAg and bPDMS-coated CC-AcOAg.

#### 4.4.2 Thermal dependence decomposition and suppressed sintering

To suppress sintering, RS-AcOAg and CC-AcOAg were coated with bPDMS as bPDMS-coated RS-AcOAg and bPDMS-coated CC-AcOAg, respectively. The morphological profiles and silver particles growth of bPDMS-coated RS-AcOAg and bPDMS-coated CC-AcOAg were investigated by SEM with thermal dependence decomposition at RT, 200°C, 250°C, and 300°C. At room temperature, the shape of bPDMS-coated RS-AcOAg and bPDMS-coated CC-AcOAg were rod shape and columnar shape, respectively (Figures 4.17 (A1 and B1)). When the temperature was raised to 200°C,  $0.11\pm 0.02$   $\mu\text{m}$  silver nanoparticles (AgNPs) were formed and presented as small particles on RS-AcOAg surfaces (Figure 4.17A2). On the other hand,  $0.11\pm 0.03$   $\mu\text{m}$  AgNPs were partially formed on edges of bPDMS-coated CC-AcOAg (Figure 4.17B2). After the temperature increased to 250°C, AgNPs of both bPDMS-coated RS-AcOAg and bPDMS-coated CC-AcOAg were grew up with the same size as  $0.18\pm 0.05$   $\mu\text{m}$  and  $0.18\pm 0.03$   $\mu\text{m}$ , respectively (Figures 4.17 (A3 and B3)). Finally, when the temperature was raised to 300°C, AgNPs size of both PDMS-coated RS-AcOAg and bPDMS-coated CC-AcOAg were slightly increase as  $0.24\pm 0.07$   $\mu\text{m}$  and  $0.26\pm 0.07$   $\mu\text{m}$ , respectively (Figures 4.17 (A4 and B4)).



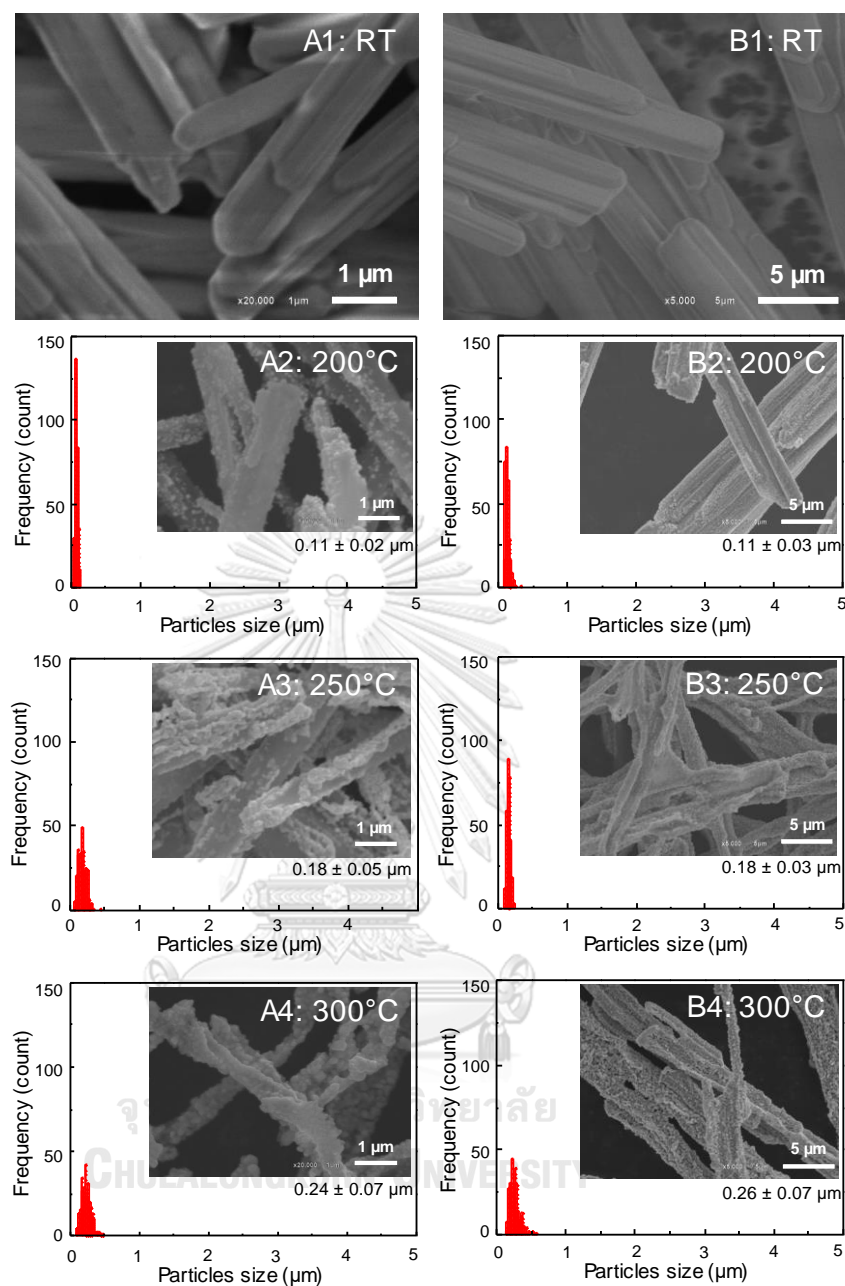


Figure 4.17 Size distribution of AgMPs obtained by decomposition of (A) bPDMS-coated RS-AgOAc and (B) bPDMS-coated CC-AgOAc at 200°C, 250°C, and 300°C.

To study the molecular information of bPDMS-coated RS-AcOAg and bPDMS-coated CC-AcOAg with thermal dependence decomposition at RT, 200°C, 250°C, and 300°C, FTIR technique was used for characterization (Figure 4.18 (A and B)). FTIR spectra of bPDMS-coated RS-AcOAg and bPDMS-coated CC-AcOAg show characteristic peaks of AcOAg as asymmetric C-O stretching ( $1592\text{ cm}^{-1}$ ), symmetric C-O stretching ( $1420\text{ cm}^{-1}$ ), symmetric  $\text{CH}_3$  deformation ( $1350\text{ cm}^{-1}$ ), in plane  $\text{CH}_3$  rocking ( $1020\text{ cm}^{-1}$ ), C-C stretching ( $930\text{ cm}^{-1}$ ), O-C-O bending ( $660\text{ cm}^{-1}$ ), and out of plane O-C-O ( $620\text{ cm}^{-1}$ ) [66] and also show characteristic peaks of bPDMS as C-H stretching ( $2905\text{ cm}^{-1}$ ), symmetric C-H bending ( $1257\text{ cm}^{-1}$ ), Si-O-Si stretching ( $1053\text{ cm}^{-1}$ ,  $1009\text{ cm}^{-1}$ ), C-H rocking ( $843\text{ cm}^{-1}$ ), and Si-C stretching ( $787\text{ cm}^{-1}$ ,  $688\text{ cm}^{-1}$ ) [72]. When the temperature was increased to 200°C and 250°C, both bPDMS-coated RS-AcOAg and bPDMS-coated CC-AcOAg show the same characteristic peaks, thus, bPDMS-coated RS-AcOAg and bPDMS-coated CC-AcOAg were not completely decomposed and the AcOAg and bPDMS remained at those temperatures. However, when the temperature was at 300°C, AcOAg was completely decomposed to form silver metal as porous silver structures. However, characteristic peaks of bPDMS remained in the porous silver structures even if they were decomposed at 300°C. These results confirmed that bPDMS was still coated on the surface of porous structures without decomposition due to its thermal stability as shown in TG thermogram of bPDMS (Figure 10). Moreover, the same characteristic peaks of bPDMS at RT and 300°C implied that bPDMS was coated on surface of porous structures as a surface stabilizer [73-74] without chemical reaction.

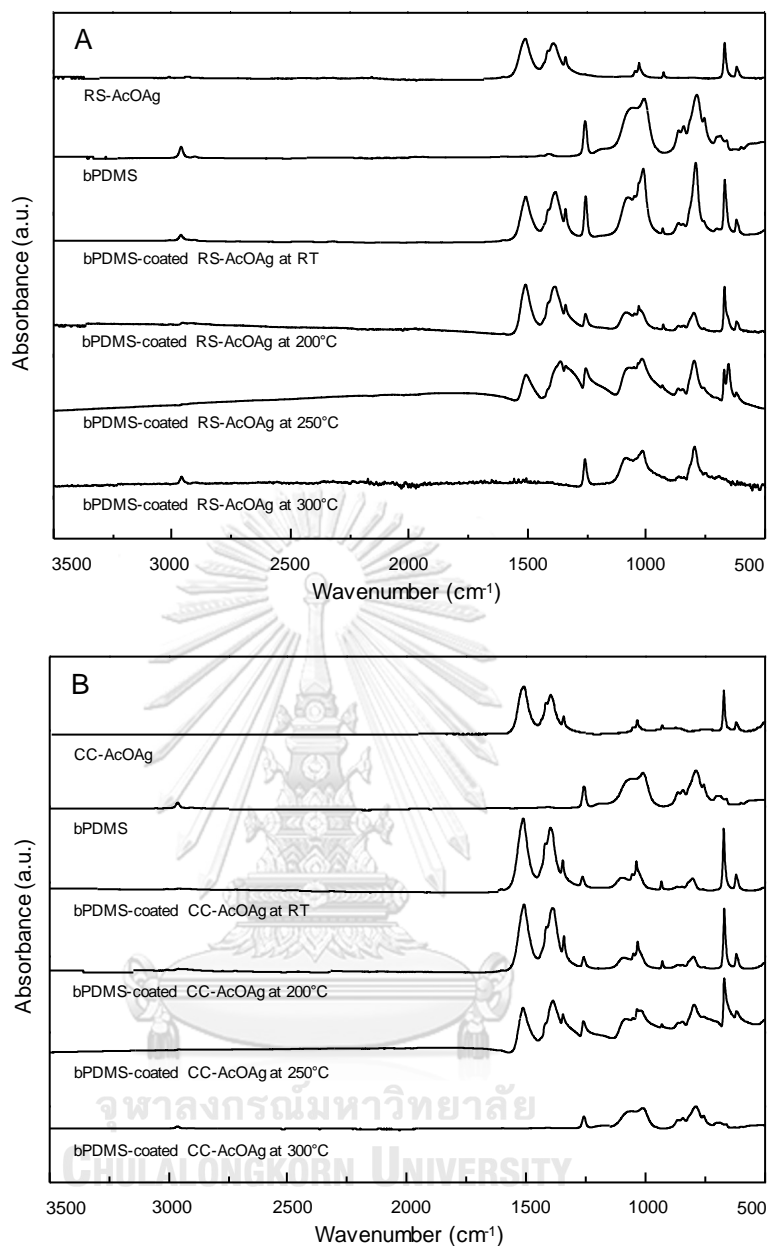


Figure 4.18 FTIR spectra of thermal dependence decomposition of (A) bPDMS-coated RS-AcOAg and (B) bPDMS-coated CC-AcOAg at RT, 200°C, 250°C, and 300°C.

#### 4.4.3 The morphology of porous silver structures

To compare the structures of porous silver structures with and without coating with bPDMS, the SEM micrographs of RS-AcOAg, bPDMS-coated RS-AcOAg, CC-AcOAg, and bPDMS-coated CC-AcOAg after thermal decomposition were taken. When RS-AcOAg and CC-AcOAg were thermally decomposed, the porous silver

structures were extensively sintered (Figures 4.19 (A1 and B1)) due to fusing of silver particles. On the other hand, bPDMS-coated RS-AcOAg and bPDMS-coated CC-AcOAg after thermally decomposed, were remaining in rod and columnar shape, respectively (Figures 4.19 (A2 and B2)) due to bPDMS suppressed the sintering of silver microparticles (AgMPs).

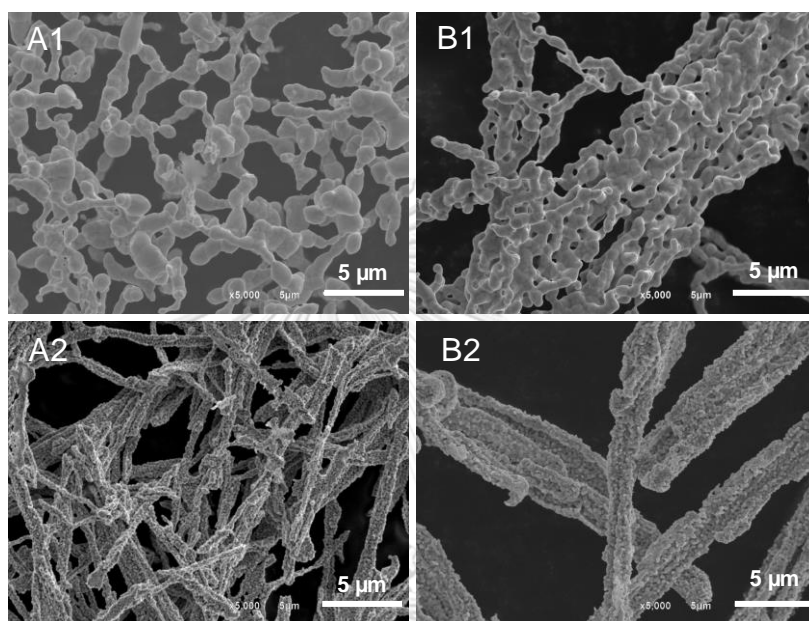


Figure 4.19 SEM micrographs of the porous silver structures of (A1) RS-AcOAg, (A2) bPDMS-coated RS-AcOAg, (B1) CC-AcOAg, and (B2) bPDMS-coated CC-AcOAg after thermal decomposition.

#### 4.4.4 The morphology of microparticles (AgMPs)

The morphology of AgMPs from porous structures of RS-AcOAg, bPDMS-coated RS-AcOAg, CC-AcOAg, and bPDMS-coated CC-AcOAg after thermal decomposition at 300°C were investigated by using SEM technique. The particle sizes of AgMPs were directly measured from SEM micrographs by ImageJ software and the size distribution histograms were subsequently created. AgMPs of thermally decomposed RS-AcOAg and CC-AcOAg possessed the average sizes about  $0.95 \pm 0.16 \mu\text{m}$  and  $2.3 \pm 0.46 \mu\text{m}$ , respectively (Figures 4.20 (A1 and B1)). The conductive material with high aspect ratio tends to have a high thermal conductivity [75-76]. The thermal conductive property along the rod axis are very different from

the transverse direction. It directly affects the thermal conductivity of the material [77]. Therefore, the RS-AcOAg with higher aspect ratio and high thermal conductivity was uniformly thermal decomposed and generated uniform AgMPs size when compared to the various AgMPs size on CC-AcOAg.

Interestingly, thermally decomposed of bPDMS-coated on both RS-AcOAg and CC-AcOAg exhibited essentially the same average AgMPs sizes which were  $0.24\pm 0.07\ \mu\text{m}$  and  $0.26\pm 0.07\ \mu\text{m}$ , respectively (Figures 4.20 (A2 and B2)). In addition, the average size of AgMPs sizes and the size distributions of bPDMS-coated RS-AcOAg and bPDMS-coated CC-AcOAg significantly decreased when compared to those of RS-AcOAg and CC-AcOAg. It is possible that bPDMS could suppress the excessive sintering of AgNPs during the thermal decomposition of bPDMS-coated RS-AcOAg and bPDMS-coated CC-AcOAg due to the interfacial phenomena between AcOAg surfaces and bPDMS film. bPDMS film played an important role as a surface stabilizer for reducing sintering of AgMPs. Normally, when AcOAg was thermally decomposed, the AgMPs were generated on the surfaces of AcOAg and fused together to form the sintering structure. When bPDMS film was employed, silver particles generated during the thermal decomposition of AgOAc were immediately coated by bPDMS film. Therefore, the aggregation and fusion between neighboring AgMPs were suppressed.

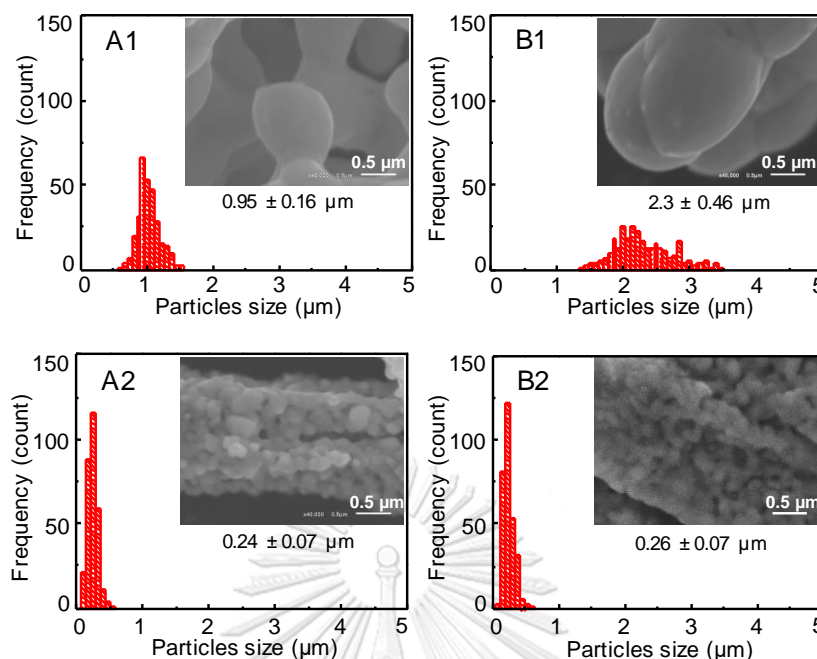


Figure 4.20 Size distribution histograms of AgMPs after thermal decomposition of (A1) RS-AgOAc, (A2) bPDMS-coated RS-AcOAg, (B1) CC-AgOAc, and (B2) bPDMS-coated RS-AcOAg.

#### 4.4.5 The surface areas of porous silver structures

To compare surface areas of porous silver structures with and without suppressed sintering by bPDMS, BET analysis was used. The surface areas of porous silver structures from thermal decomposition of RS-AcOAg and CC-AcOAg were  $2.05 \text{ m}^2/\text{g}$  and  $1.36 \text{ m}^2/\text{g}$ , respectively. On the other hand, the surface areas of porous silver structures from thermal decomposition of bPDMS-coated RS-AcOAg and bPDMS-coated CC-AcOAg were  $3.43 \text{ m}^2/\text{g}$  and  $2.37 \text{ m}^2/\text{g}$ , respectively (Table 4.3). It can conclude that the surface areas of porous silver structures from thermal decomposition of RS-AcOAg and CC-AcOAg increased to 67% and 74%, respectively, after they were suppressed sintering by bPDMS. The surface areas of porous silver structures, which were suppressed sintering, increased due to the smaller size of AgMPs.



Table 4.3 The surface areas of porous silver structures.

Source of porous silver	Surface area (m <sup>2</sup> /g)
RS-AcOAg	2.05
bPDMS-coated RS-AcOAg	3.42
CC-AcOAg	1.36
bPDMS-coated CC-AcOAg	2.37

#### 4.4.6 Elemental analysis

In this work, chemical compositions before and after thermal decomposition of RS-AcOAg, bPDMS-coated RS-AcOAg, CC-AcOAg, and bPDMS-coated CC-AcOAg after thermal decomposition at 300°C were studied by using the energy-dispersive X-ray spectroscopy (EDS) mode of SEM (point analysis).

Focusing on the percentage of silver atom of RS-AcOAg increased from 22.14% to 80.29% after thermal decomposition, whereas the percentage of carbon atom decreased from 76.52% to 17.99% (Figures 4.21 (A and B)). On the other hand, bPDMS-coated RS-AcOAg after thermally decomposed the percentage of silver atom increased from 20.55% to 72.14%, whereas the percentage of carbon atom decreased from 57.56% to 24.56% and the percentage of silicon atom decreased from 9.47% to 1.56% (Figures 4.21 (C and D)).

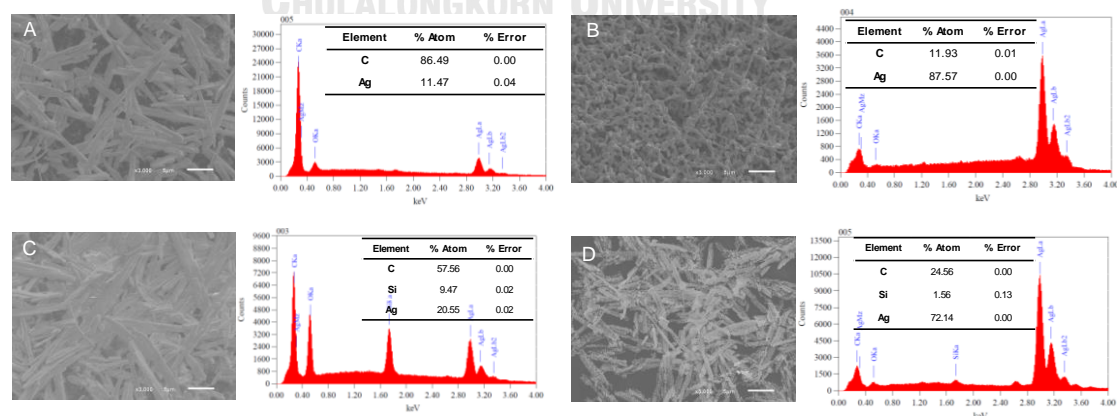


Figure 4.21 SEM-EDX point analysis of (A) RS-AcOAg, (B) after thermally decomposed RS-AcOAg, (C) bPDMS-coated RS-AcOAg, and (D) after thermally decomposed bPDMS-coated RS-AcOAg.

SEM-EDX info of CC-AcOAg and bPDMS-coated CC-AcOAg before and after thermal decomposition were presented in Figure 4.22. The percentage of silver atom of CC-AcOAg increased from 26.29% to 85.21%, whereas the percentage of carbon atom decreased from 72.47% to 13.53% (Figures 4.22 (A and B)). After bPDMS-coated CC-AcOAg was thermally decomposed to porous silver structure, the percentage of silver atom increased from 21.13% to 72.89% and the percentage of silicon atom increased from 1.45% to 2.76%, while the percentage of carbon atom decreased from 72.69% to 18.47% (Figures 4.22 (C and D)).

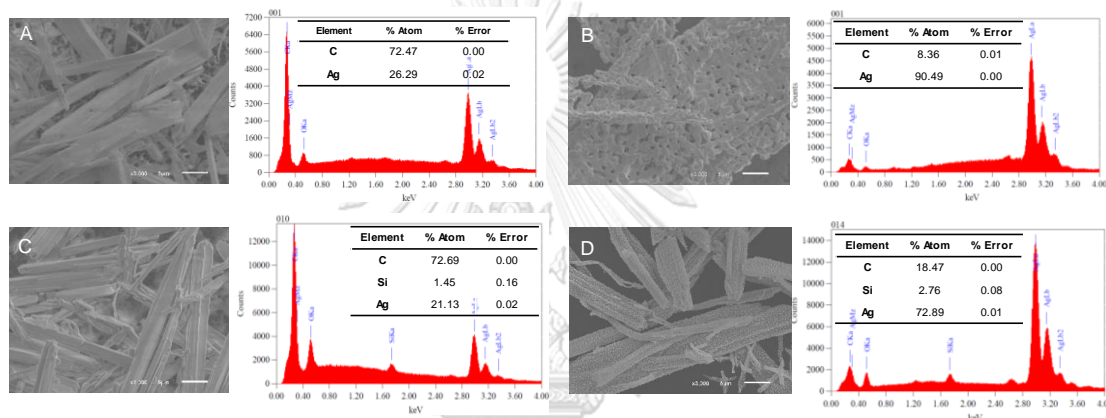


Figure 4.22 SEM-EDX point analysis of (A) CC-AcOAg, (B) thermally decomposed CC-AcOAg, (C) bPDMS-coated CC-AcOAg, and (D) thermally decomposed bPDMS-coated CC-AcOAg.

The SEM-EDX info (Figures 4.21-4.22) presented that the percentage of carbon atom from all samples were not decomposed to 0% due to an acetic acid residue was remaining after thermal decomposition of the AcOAg as presented in Eq.7. These results implied that RS-AcOAg, bPDMS-coated RS-AcOAg, CC-AcOAg and bPDMS-coated CC-AcOAg were thermally decomposed at 300°C to porous silver structures.

According to the characterization, we can conclude that RS-AcOAg and CC-AcOAg are the same materials based on FTIR spectra, Raman spectra, and XRD patterns. However, the aspect ratio of RS-AcOAg is 23% higher than CC-AcOAg and tends to have a high thermal conductivity. In addition, the AgMPs size of thermal decomposition morphology of RS-AcOAg and CC-AcOAg were different as

$0.95\pm 0.16\ \mu\text{m}$  and  $2.3\pm 0.46\ \mu\text{m}$  respectively. After the porous silver structures from RS-AcOAg and CC-AcOAg were film coated by bPDMS, the size of AgMPs decreased to  $0.24\pm 0.07\ \mu\text{m}$  and  $0.26\pm 0.07\ \mu\text{m}$ , respectively, because bPDMS was aimed as a surface stabilizer to suppress sintering of AgMPs during thermally decomposed. Moreover, the surface areas of porous silver structures from RS-AcOAg, which was suppressed sintering, is higher than that of CC-AcOAg due to the smaller size of AgMPs. Herein, RS-AcOAg and bPDMS-coated RS-AcOAg were selected to employ as a raw material for the fabrication of PDMS-silver composite as flexible conductive strips and comparison of electrical resistivity.

To compare the morphological structures of RS-AcOAg and bPDMS-coated RS-AcOAg after thermal decomposition the SEM was used for investigated. The porous silver structures from thermally decomposed of RS-AcOAg (Figure 4.23A) showed the sintered structures. In contrast, porous silver structure from thermally decomposed of bPDMS-coated RS-AcOAg (Figure 4.23B) remained in the rod shape with suppressed sintering. The porous structure from thermally decomposed RS-AcOAg with sintered structure tended to crack under mechanical loading due to the sintered structure.

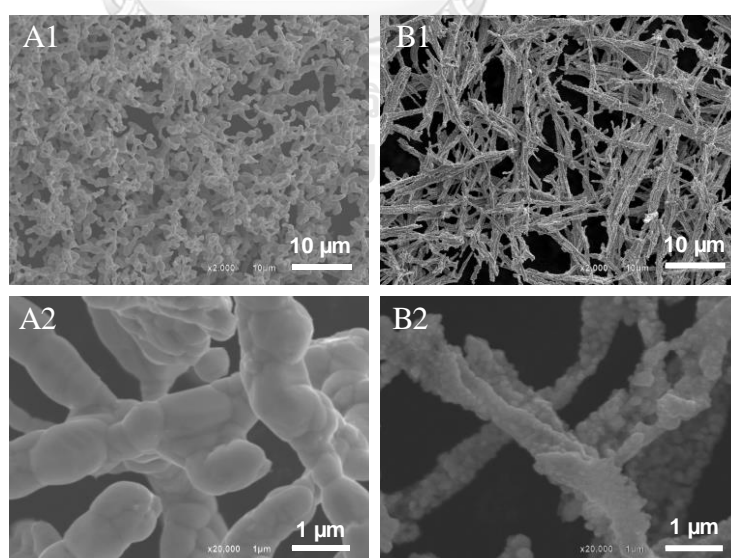


Figure 4.23 Porous silver structure of (A) RS-AcOAg and (B) bPDMS-coated RS-AcOAg after thermal decomposition at  $300^{\circ}\text{C}$ .

#### 4.5 Fabrication of PDMS-silver composite flexible conductive strips

RS-AcOAg was chosen for further PDMS-silver composite fabrication for applying as a flexible conductive strip due to the appropriate morphology, the high aspect ratio, and the suitable thermal decomposition properties when compared to CC-AcOAg. The porous silver film, which is attached on the surface of PDMS, played a crucial role in the conductive property. The existence of porous silver layer on PDMS substrate was confirmed by a chemical test. Herein,  $\text{H}_2\text{O}_2$  was dropped on the surface of the conductive strip which can interact with Ag metal and generate  $\text{O}_2$  bubbles (Figure 4.24A) from the catalytic decomposition of  $\text{H}_2\text{O}_2$  by silver metal. In contrast, there were no bubbles on the bare PDMS surface (Figure 4.24A). Additionally, the LED light was illuminated while the two-point probe multimeter was clipped on the surface of a strip (Figure 4.24B). These results implied that the porous silver was fixed on the top of PDMS substrate.



Figure 4.24 (A) Digital images of hydrogen peroxide testing, confirming that silver structures were adhered on PDMS surface after fabrication. (B) LED light testing while the two-point probe multimeter was clipped on the surface of a strip.

After the fabrication, the morphology of the porous silver on the strip under 30% strain was observed under an optical microscope. Two types of flexible conductive strips i.e. the porous silver strip from thermally decomposed RS-AcOAg (Figure 4.25A) and the porous silver strip from thermally decomposed bPDMS-coated RS-AcOAg (Figure 4.25B) were investigated. The electrical resistivity values of the porous silver strips from RS-AcOAg and bPDMS-coated RS-AcOAg at the original length were  $6.3 \Omega$  and  $5.0 \Omega$  respectively. At 30% strain, the electrical resistivity values of the porous silver strips from RS-AcOAg and bPDMS-coated RS-AcOAg

increased to  $7.6 \Omega$  and  $6.2 \Omega$ , respectively. The empty space within the porous silver structures can be observed when the strip was under 30% strain (Figures 4.25 (Ab and Bb)). The porous silver structure was recovered after stretching (Figures 4.25 (Ac and Bc)). The electrical resistivity values at the recovered state of the porous silver strips from RS-AcOAg and bPDMS-coated RS-AcOAg were  $7.6 \Omega$  and  $6.2 \Omega$ , respectively. The electrical resistivity of the porous silver strips from RS-AcOAg at the recovered state was slightly increased due to the sintered structure was cracking after applying the strain loading. On the other hand, the electrical resistivity of the porous silver strips from bPDMS-coated RS-AcOAg was invariable under 30% strain.

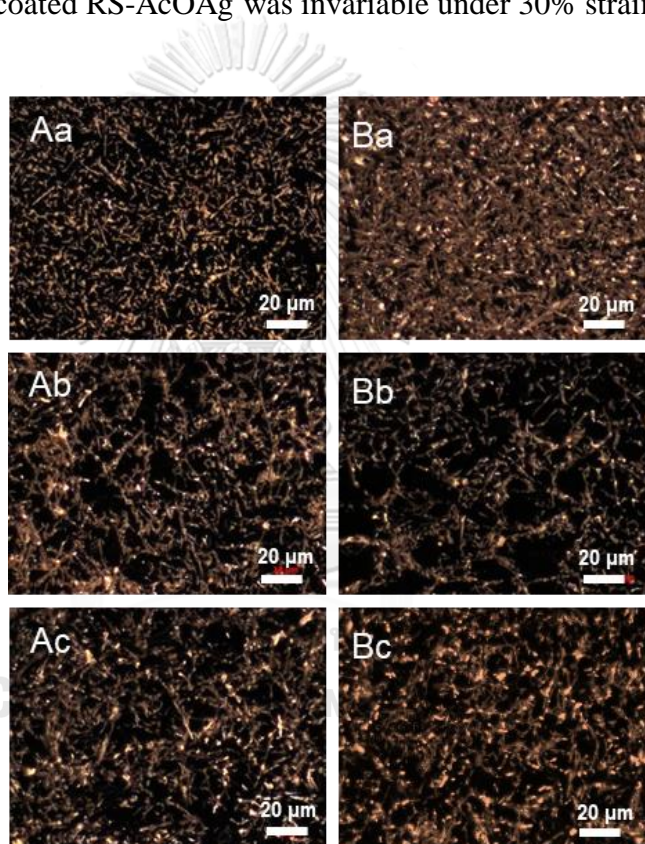


Figure 4.25 Optical microscope images of PDMS-silver composite as the porous silver strips from (A) RS-AcOAg and (B) bPDMS-coated RS-AcOAg; (Aa, Ba) original film ( $R=6.3 \Omega$ ,  $5.0 \Omega$ ), (Ab, Bb) during under strain ( $R=7.6 \Omega$ ,  $6.2 \Omega$ ), and (Ac, Bc) after releasing strain ( $R=7.0 \Omega$ ,  $5.0 \Omega$ ). The strips were under 30% strain.

To measure the electrical resistivity of the porous silver strips, the electrical resistivity was measured under the relative changes of the resistance ( $\Delta R/R_0$ ) where  $\Delta R/R_0 = (R-R_0)/R_0$ ,  $R_0$  is the electrical resistance of the strip before applied mechanical strain, and  $R$  is the resistance while applied the mechanical strain.

The relative changes of the resistance ( $\Delta R/R_0$ ) under continuously monitored during applied mechanical strain (Figure 4.26A), bending (Figure 4.26B), and twisting (Figure 4.26C) increased when the mechanical strain was applied to the strips. As expected, the porous silver strips from bPDMS-coated RS-AcOAg (red line) displayed the lowest relative changes of the resistance. The porous silver strips from RS-AcOAg (black line) had higher relative changes of the resistance compared to the porous silver strips from bPDMS-coated RS-AcOAg (red line) due to internal cracking of sintered structure under mechanical loading [36]. The evaporated silver strip (blue line), which was thermally evaporated a 150  $\mu\text{m}$  thickness of silver metal on PDMS substrate by thermal evaporator was using a benchmark. It displayed the highest relative changes of the resistance due to cracking of silver metal. For twisting condition, when the force was applied on the strips, the relative changes of the resistance (Figure 4.26C) increased significantly compared to stretching and bending because the twisting generated more cracking points in the porous silver structures.



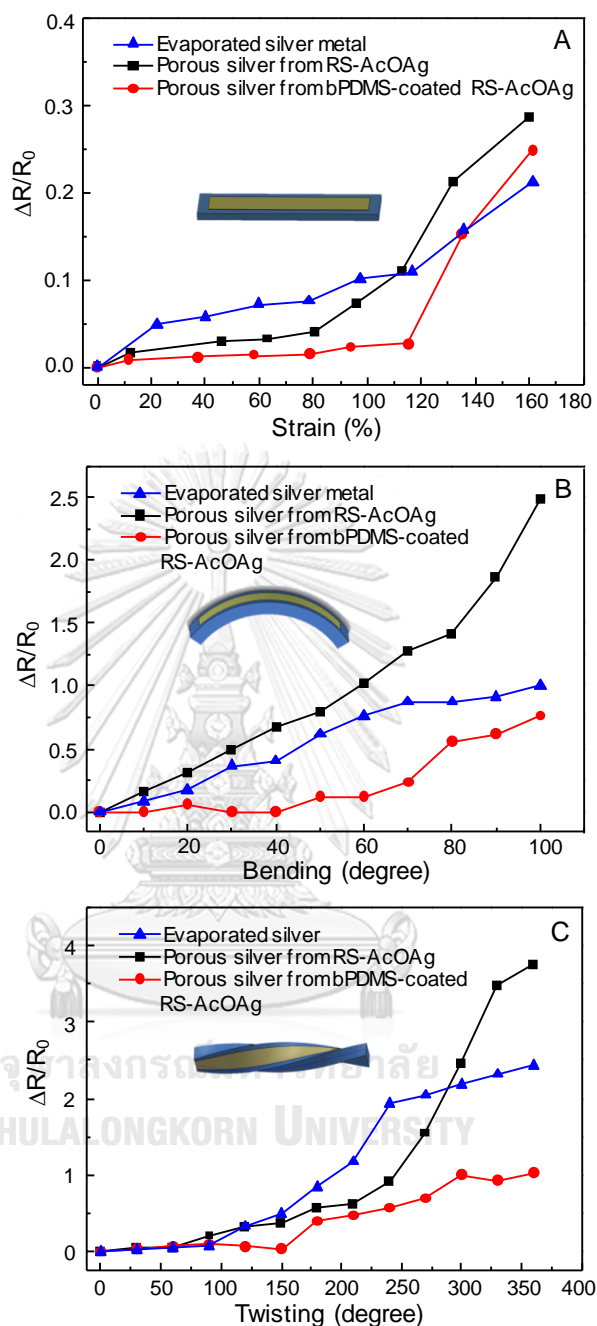
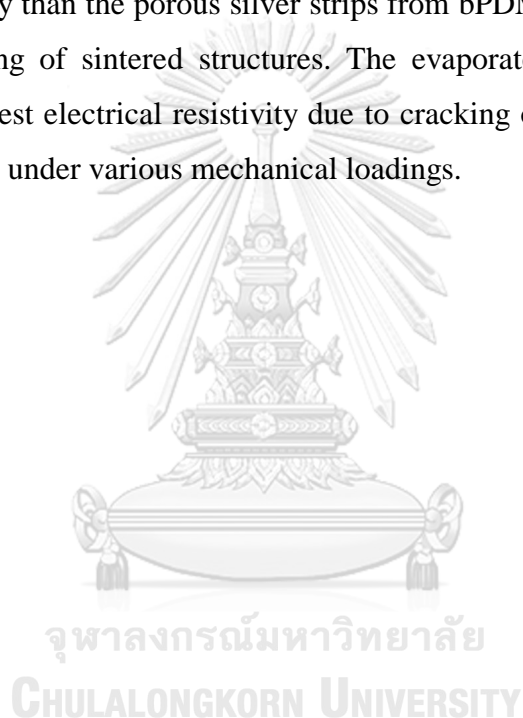


Figure 4.26 Relative changes of electrical resistance ( $\Delta R/R_0$ ) under continuously applied the mechanical force with (A) stretching, (B) bending, and (C) twisting of flexible conductive strips. The blue, black, and red lines were represented the relative change of evaporated silver strip, porous silver strip from RS-AcOAg, and porous silver strip from bPDMS coated RS-AcOAg, respectively.

The relative changes of electrical resistance ( $\Delta R/R_0$ ) under cyclic mechanical loadings at 30% stretching (Figure 4.27A), 90° bending (Figure 4.27B), and 180° twisting were shown in Figure 4.27C. The relative changes of electrical resistivity under cyclic mechanical loadings exhibited the same trend as continuous mechanical loadings. The porous silver strip from bPDMS-coated RS-AcOAg (red line) showed the lowest values and the highest consistency in relative changes of electrical resistivity after each mechanical loading cycle due to suppress sintering structure by bPDMS. The porous silver strip from RS-AcOAg (black line) exhibited higher electrical resistivity than the porous silver strips from bPDMS-coated RS-AcOAg due to internal cracking of sintered structures. The evaporated silver strip (blue line) displayed the highest electrical resistivity due to cracking of silver metal film on the surface of the strip under various mechanical loadings.





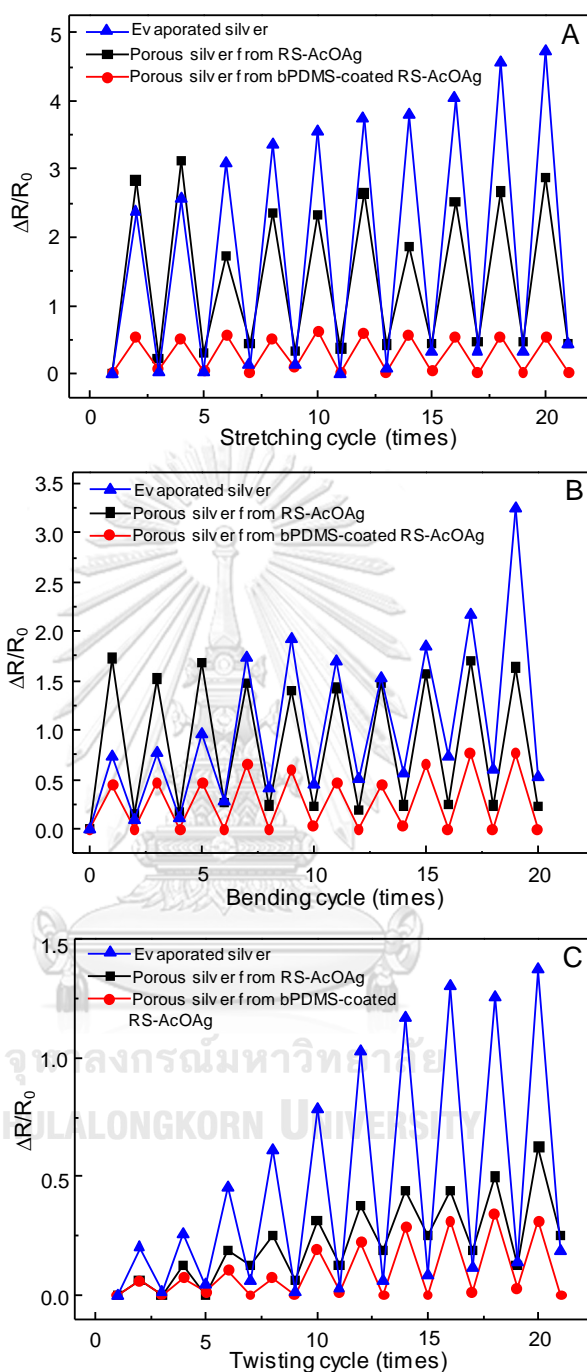


Figure 4.27 Relative changes of electrical resistance ( $\Delta R/R_0$ ) under cyclically applied mechanical loadings with (A) 30% strain, (B) 90° bending, and (C) 180° twisting of flexible conductive strips. The values for evaporated silver strip, porous silver strip from RS-AcOAg, and porous silver strip from bPDMS-coated RS-AcOAg are shown in blue, black, and red lines, respectively.

From the relative changes of electrical resistance, the porous silver strip from bPDMS-coated RS-AcOAg exhibited the excellent mechanical properties with low electrical resistivity under mechanical strain, including stretching, bending, and twisting. To compare the  $\Delta R/R_0$  of the porous silver strip from bPDMS-coated RS-AcOAg to the other works, we found that the  $\Delta R/R_0$  of the porous silver strip which fabricated in this study had lower  $\Delta R/R_0$  than AgNWs/PDMS [12] and silver ink/PDMS [13] under applying mechanical forces including strain and bending.

Furthermore, the porous silver strip from bPDMS-coated RS-AcOAg with 4 cm length was employed as a flexible conductive polymer and preliminarily demonstrated with LED devices (Figure 4.28). According to visual observations, the LED exhibited significant brightness under 30% strain (Figure 4.28A), 90° bending (Figure 4.28B), and 180° twisting (Figure 4.28C). In addition, the strip could also be applying as a strain sensor for controlling a robotic arm movement (Figure 4.29).

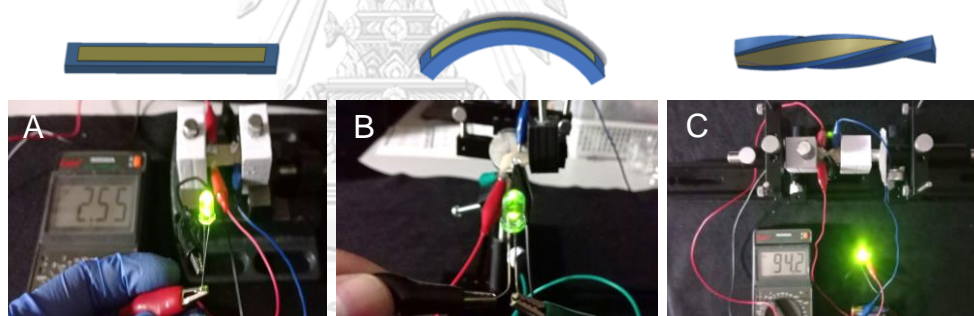


Figure 4.28 LED applications of porous silver conductive strip from bPDMS-coated RS-AcOAg. Photographic images of working LEDs under (A) 30% strain, (B) 90° bending, and (C) 180° twisting loads.

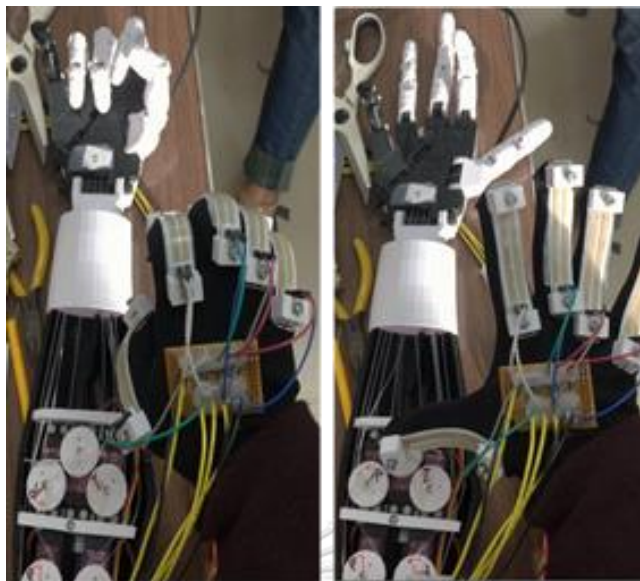


Figure 4.29 The strain sensor fabricated from the porous silver strip of bPDMS-coated RS-AcOAg for controlling robotic arm movement.



## CHAPTER V

### CONCLUSIONS

In this research, a simple and low-cost synthetic protocol for fabricating PDMS-silver composite as flexible conductive strips is presented. To form conductive materials, the small amount of AcOAg, which is required for fabricating flexible conductive polymer, is only 10% w/w, was thermally decomposed at 300°C. The thermal decomposition of AcOAg induced the formation of AgMPs on the surface of AcOAg with the expense of AcOAg and turned into sintered and rigid structures. The sintered structures affected the electrical resistivity due to the cracking of structures when mechanical strain was applied. To suppress sintering structure, bPDMS was employed for film coating on the surface of AcOAg before thermal decomposition. The bPDMS film also played an important role in a surface stabilizer. The sintering of AgMPs was reduced because silver particles, which was forming during the thermal decomposition of AgOAc, were immediately coated by bPDMS film. Hence, the aggregation and fusion between neighboring AgMPs were suppressed. Herein, silver acetate crystals, which was obtained by synthesis (RS-AcOAg) and commercial (CC-AcOAg), were used in this study for comparing the dimension, morphological structures, molecular information, and chemical composition. There were no significant differences in molecular information and chemical composition. However, the size of RS-AcOAg is 3-times smaller than CC-AcOAg whereas the aspect ratio of RS-AcOAg is 23% higher than CC-AcOAg, suggesting that the electrical conductivity properties of RS-AcOAg tends to be better than CC-AcOAg [65]. Moreover, the surface area of porous silver structure of RS-AcOAg, which was suppressed sintering by bPDMS coating, was higher than that of CC-AcOAg. Thus, RS-AcOAg was chosen to employ as a raw material for conductive materials fabrication under suppressed sintering by coating with bPDMS as bPDMS-coated RS-AcOAg. To form the flexible conductive strip, bPDMS-coated RS-AcOAg was thermally decomposed at 300°C to form porous silver films. Then, the mixture of PDMS base and curing agent was poured on the porous silver films. After curing process, a flexible conductive strip was cut and detached from supporting surface. The

flexible conductive strip from bPDMS-coated RS-AcOAg exhibited excellent mechanical properties with low electrical resistivity under applied mechanical strain, including stretching, bending, and twisting. Herein, an application of the PDMS-silver composite as a flexible conductive strip to use as a strain sensor for robotic hand was demonstrated.

For further development of this research, the simple and low-cost synthetic protocol for fabricating PDMS-silver composite can be applied in flexible circuit boards instead of general circuit boards. The advantages of flexible circuit boards are their conductive efficiency under mechanical stress, space saving, low production costs and their suitability for current electrical equipment design.



## REFERENCES

1. Bradley, K.; Gabriel, J. C. P.; Grüner, G., Flexible Nanotube Electronics. *Nano Letters* **2003**, *3* (10), 1353-1355.
2. Maliakal, A.; Katz, H.; Cotts, P. M.; Subramoney, S.; Mirau, P., Inorganic Oxide Core, Polymer Shell Nanocomposite as a High K Gate Dielectric for Flexible Electronics Applications. *Journal of the American Chemical Society* **2005**, *127* (42), 14655-14662.
3. Jung, Y. J.; Kar, S.; Talapatra, S.; Soldano, C.; Viswanathan, G.; Li, X.; Yao, Z.; Ou, F. S.; Avadhanula, A.; Vajtai, R.; Curran, S.; Nalamasu, O.; Ajayan, P. M., Aligned Carbon Nanotube–Polymer Hybrid Architectures for Diverse Flexible Electronic Applications. *Nano Letters* **2006**, *6* (3), 413-418.
4. Lee, P.; Lee, J.; Lee, H.; Yeo, J.; Hong, S.; Nam, K. H.; Lee, D.; Lee, S. S.; Ko, S. H., Highly Stretchable and Highly Conductive Metal Electrode by Very Long Metal Nanowire Percolation Network. *Advanced Materials* **2012**, *24* (25), 3326-3332.
5. Matsuzaki, R.; Tabayashi, K., Highly Stretchable, Global, and Distributed Local Strain Sensing Line Using GaInSn Electrodes for Wearable Electronics. *Advanced Functional Materials* **2015**, *25* (25), 3806-3813.
6. Jeon, J. Y.; Ha, T. J., Waterproof Electronic-Bandage with Tunable Sensitivity for Wearable Strain Sensors. *ACS Applied Materials & Interfaces* **2016**, *8* (4), 2866-2871.
7. Casu, M. R., Improving Synchronous Elastic Circuits: Token Cages and Half-Buffer Retiming, 2010 IEEE Symposium on Asynchronous Circuits and Systems, 3-6 May 2010; **2010**, 128-137.
8. Chen, J.; Zheng, J.; Gao, Q.; Zhang, J.; Zhang, J.; Omisore, M. O.; Wang, L.; Li, H., Polydimethylsiloxane (PDMS)-Based Flexible Resistive Strain Sensors for Wearable Applications. *Applied Sciences* **2018**, *8* (3), 345-359. doi: 10.3390/app8030345
9. Peng, P.; Wu, K.; Lv, L.; Guo, C. F.; Wu, Z., One-Step Selective Adhesive Transfer Printing for Scalable Fabrication of Stretchable Electronics. *Advanced Materials Technologies* **2018**, 1700264-1700270. doi: 10.1002/admt.201700264
10. Kim, K. S.; Lee, Y. C.; Ahn, J. H.; Jung, S. B., Evaluation of the Flexibility of

- Silver Circuits Screen-Printed on Polyimide with an Environmental Reliability Test. *Journal of nanoscience and nanotechnology* **2011**, *11* (7), 5806-5811.
11. Nie, X.; Wang, H.; Zou, J., Inkjet Printing of Silver Citrate Conductive Ink on PET Substrate. *Applied Surface Science* **2012**, *261*, 554-560.
  12. Chou, N.; Kim, Y.; Kim, S., A Method to Pattern Silver Nanowires Directly on Wafer-Scale PDMS Substrate and Its Applications. *ACS Applied Materials & Interfaces* **2016**, *8* (9), 6269-6276.
  13. Li, C. Y.; Liao, Y. C., Adhesive Stretchable Printed Conductive Thin Film Patterns on PDMS Surface with an Atmospheric Plasma Treatment. *ACS Applied Materials & Interfaces* **2016**, *8* (18), 11868-11874.
  14. Zhang, L.; Zhang, L.; Qiu, Y.; Ji, Y.; Liu, Y.; Liu, H.; Li, G.; Guo, Q., Improved Performance by SiO<sub>2</sub> Hollow Nanospheres for Silver Nanowire-Based Flexible Transparent Conductive Films. *ACS Applied Materials & Interfaces* **2016**, *8* (40), 27055-27063.
  15. Zope, K. R.; Cormier, D.; Williams, S. A., Reactive Silver Oxalate Ink Composition with Enhanced Curing Conditions for Flexible Substrates. *ACS Applied Materials & Interfaces* **2018**, *10* (4), 3830-3837.
  16. Wangping, H.; Jinhui, L.; Songfang, Z.; Fei, H.; Guoping, Z.; Rong, S.; Ching Ping, W., Highly Electrically Conductive and Stretchable Copper Nanowires-Based Composite for Flexible and Printable Electronics. *Composites Science and Technology* **2017**, *146*, 169-176.
  17. Pan, C.; Kumar, K.; Li, J.; Markvicka, E. J.; Herman, P. R.; Majidi, C., Visually Imperceptible Liquid-Metal Circuits for Transparent, Stretchable Electronics with Direct Laser Writing. *Advanced Functional Materials* **2018**. doi: 10.1002/adma.201706937
  18. Jakubowska, M.; Słoma, M.; Młozniak, A., Printed Transparent Electrodes Containing Carbon Nanotubes For Elastic Circuits Applications With Enhanced Electrical Durability Under Severe Conditions. *Materials Science and Engineering: B* **2011**, *176* (4), 358-362.
  19. Lei, T.; Pochorovski, I.; Bao, Z., Separation of Semiconducting Carbon Nanotubes for Flexible and Stretchable Electronics Using Polymer Removable Method.

- Accounts of chemical research* **2017**, *50* (4), 1096-1104.
20. Yao, H. B.; Ge, J.; Wang, C. F.; Wang, X.; Hu, W.; Zheng, Z. J.; Ni, Y.; Yu, S. H., A Flexible and Highly Pressure-Sensitive Graphene–Polyurethane Sponge Based on Fractured Microstructure Design. *Advanced Materials* **2013**, *25* (46), 6692-6698.
  21. Li, J.; Liu, Q.; Ho, D.; Zhao, S.; Wu, S.; Ling, L.; Han, F.; Wu, X.; Zhang, G.; Sun, R.; Wong, C. P., Three-Dimensional Graphene Structure for Healable Flexible Electronics based on Diels-Alder Chemistry. *ACS Applied Materials & Interfaces* **2018**, 1-25.
  22. He, L.; Tjong, S. C., Facile Synthesis of Silver-Decorated Reduced Graphene Oxide As a Hybrid Filler Material for Electrically Conductive Polymer Composites. *RSC Advances* **2015**, *5* (20), 15070-15076.
  23. Chen, Z.; Ren, W.; Gao, L.; Liu, B.; Pei, S.; Cheng, H. M., Three-Dimensional Flexible and Conductive Interconnected Graphene Networks Grown by Chemical Vapour Deposition. *Nature Materials* **2011**, *10*, 424-428.
  24. Sun, J.; Jiang, J.; Bao, B.; Wang, S.; He, M.; Zhang, X.; Song, Y., Fabrication of Bendable Circuits on a Polydimethylsiloxane (PDMS) Surface by Inkjet Printing Semi-Wrapped Structures. *Materials* **2016**, *9* (4), 253-266.
  25. Liu, H. S.; Pan, B. C.; Liou, G. S., Highly Transparent AgNW/PDMS Stretchable Electrodes for Elastomeric Electrochromic Devices. *Nanoscale* **2017**, *9* (7), 2633-2639.
  26. Azoubel, S.; Magdassi, S., Controlling Adhesion Properties of SWCNT–PET Films Prepared by Wet Deposition. *ACS Applied Materials & Interfaces* **2014**, *6* (12), 9265-9271.
  27. Kim, I.; Woo, K.; Zhong, Z.; Lee, E.; Kang, D.; Jeong, S.; Choi, Y.-M.; Jang, Y.; Kwon, S.; Moon, J., Selective Light-Induced Patterning of Carbon Nanotube/Silver Nanoparticle Composite To Produce Extremely Flexible Conductive Electrodes. *ACS Applied Materials & Interfaces* **2017**, *9* (7), 6163-6170.
  28. Hu, W.; Wang, R.; Lu, Y.; Pei, Q., An Elastomeric Transparent Composite Electrode Based on Copper Nanowires and Polyurethane. *Journal of Materials Chemistry C* **2014**, *2* (7), 1298-1305.
  29. Larmagnac, A.; Eggenberger, S.; Janossy, H.; Voros, J., Stretchable Electronics



- Based on Ag-PDMS Composites. *Scientific reports* **2014**, *4*, 7254-7260.  
doi: 10.1038/srep07254
30. Hu, Y.; Zhao, T.; Zhu, P.; Zhu, Y.; Shuai, X.; Liang, X.; Sun, R.; Lu, D. D.; Wong, C. P., Low Cost and Highly Conductive Elastic Composites for Flexible and Printable Electronics. *Journal of Materials Chemistry C* **2016**, *4* (24), 5839-5848.
  31. Costa, T. H.; Choi, J. W., A Flexible Two Dimensional Force Sensor Using PDMS Nanocomposite. *Microelectronic Engineering* **2017**, *174*, 64-69.
  32. Hansen, T. S.; West, K.; Hassager, O.; Larsen, N. B., Highly Stretchable and Conductive Polymer Material Made from Poly(3,4-ethylenedioxythiophene) and Polyurethane Elastomers. *Advanced Functional Materials* **2007**, *17* (16), 3069-3073.
  33. Kim, J.; Park, J.; Jeong, U.; Park, J. W., Silver Nanowire Network Embedded in Polydimethylsiloxane as Stretchable, Transparent, and Conductive Substrates. *Journal of Applied Polymer Science* **2016**, *133* (33), 43830-43836.  
doi: 10.1002/app.43830
  34. Wang, H.; Shi, M. Y.; Zhu, K.; Su, Z. M.; Zhang, M.; Zhang, H. X., Fabrication of Stretchable and Flexible Vertically Aligned Carbon Nanotube Film, 2016 IEEE 11<sup>th</sup> Annual International Conference on Nano/Micro Engineered and Molecular Systems, NEMS 2016, **2016**, 482-485.
  35. Rahimi, R.; Ochoa, M.; Ziaie, B., Direct Laser Writing of Porous-Carbon/Silver Nanocomposite for Flexible Electronics. *ACS Applied Materials & Interfaces* **2016**, *8* (26), 16907-16913.
  36. Wang, M.; Chen, H.; Lin, W.; Li, Z.; Li, Q.; Chen, M.; Meng, F.; Xing, Y.; Yao, Y.; Wong, C.-p.; Li, Q., Crack-Free and Scalable Transfer of Carbon Nanotube Arrays into Flexible and Highly Thermal Conductive Composite Film. *ACS Applied Materials & Interfaces* **2014**, *6* (1), 539-544.
  37. Hu, Y.; Zhao, T.; Zhu, P.; Zhang, Y.; Liang, X.; Sun, R.; Wong, C. P.; A Printable and Flexible Conductive Polymer Composite With Sandwich Structure For Stretchable Conductor and Strain Sensor Applications, 2017 18<sup>th</sup> International Conference on Electronic Packaging Technology (ICEPT), 16-19 Aug. 2017; **2017**, 1361-1365.

38. David, S., The Independent Global Source for the Flexible and Printed Electronics Industry. *SunChemical* **2017**, 2-10.
39. Wang, Y.; Guo, H.; Chen, J. J.; Sowade, E.; Wang, Y.; Liang, K.; Marcus, K.; Baumann, R. R.; Feng, Z. S., Paper-Based Inkjet-Printed Flexible Electronic Circuits. *ACS Applied Materials & Interfaces* **2016**, 8 (39), 26112-26118.
40. Olson, L. P.; Whitcomb, D. R.; Rajeswaran, M.; Blanton, T. N.; Stwertka, B. J., The Simple Yet Elusive Crystal Structure of Silver Acetate and the Role of the Ag–Ag Bond in the Formation of Silver Nanoparticles during the Thermally Induced Reduction of Silver Carboxylates. *Chemistry of Materials* **2006**, 18 (6), 1667-1674.
41. Fey, M.; Hollander, M.; Hymowitz, N., Silver-Acetate Deterrent Therapy: A Minimal-Intervention Self-help Aid. *The Clinical Management of Nicotine Dependence*, Springer New York: New York, NY, **1991**, 150-156.
42. Kascatan, N. A.; Melaiye, A.; Hindi, K.; Durmus, S.; Panzner, M. J.; Hogue, L. A.; Mallett, R. J.; Hovis, C. E.; Coughenour, M.; Crosby, S. D.; Milsted, A.; Ely, D. L.; Tessier, C. A.; Cannon, C. L.; Youngs, W. J., Synthesis From Caffeine of a Mixed N-Heterocyclic Carbene–Silver Acetate Complex Active against Resistant Respiratory Pathogens. *Journal of Medicinal Chemistry* **2006**, 49 (23), 6811-6818.
43. Miller, J. H. (1990). *United States Patent US No. 1922387*. Retrieve from <https://patentimages.storage.googleapis.com/93/89/20/e86dc659fa4492/US1922387.pdf>
44. Dearden, A. L.; Smith, P. J.; Shin, D.-Y.; Reis, N.; Derby, B.; O'Brien, P., A Low Curing Temperature Silver Ink for Use in Ink-Jet Printing and Subsequent Production of Conductive Tracks. *Macromolecular Rapid Communications* **2005**, 26 (4), 315-318.
45. Nakano, M.; Fujiwara, T.; Koga, N., Thermal Decomposition of Silver Acetate: Physico-Geometrical Kinetic Features and Formation of Silver Nanoparticles. *The Journal of Physical Chemistry C* **2016**, 120 (16), 8841-8854.
46. Bianchini, A.; Playle, R. C.; Wood, C. M.; Walsh, P. J., Mechanism of Acute Silver Toxicity in Marine Invertebrates. *Aquatic Toxicology* **2005**, 72 (1), 67-82.
47. Qadeer, R.; Anjum, M. S.; Ikram, S.; Munir, A., Optimization of Process

- Parameters for the Production of Battery Grade Acetic Silver Powder. *Journal of the Chemical Society of Pakistan* **2003**, 25(2), 93-97.
48. Logvinenko, V.; Polunina, O.; Mikhailov, Y.; Mikhailov, K.; Bokhonov, B., Study of Thermal Decomposition of Silver Acetate. *Journal of Thermal Analysis and Calorimetry* **2007**, 90 (3), 813-816.
49. Abu Zied, B. M.; Asiri, A. M., An Investigation of the Thermal Decomposition of Silver Acetate as a Precursor for Nano-Sized Ag-Catalyst. *Thermochimica Acta* **2014**, 581, 110-117.
50. Larena Avellaneda, A.; Russmann, S.; Fein, M.; Debus, E. S., Prophylactic Use of The Silver-Acetate-Coated Graft in Arterial Occlusive Disease: A Retrospective, Comparative Study. *Journal of Vascular Surgery* **2009**, 50 (4), 790-798.
51. Jeanmonod, P.; Laschke, M. W.; Gola, N.; von Heesen, M.; Glanemann, M.; Dold, S.; Menger, M. D.; Moussavian, M. R., Silver Acetate Coating Promotes Early Vascularization of Dacron Vascular Grafts Without Inducing Host Tissue Inflammation. *Journal of Vascular Surgery* **2013**, 58 (6), 1637-1643.
52. Tao, Y.; Tao, Y.; Wang, B.; Wang, L.; Tai, Y., A Facile Approach to a Silver Conductive Ink With High Performance for Microelectronics. *Nanoscale Research Letters* **2013**, 8 (1), 296-301.
53. Ristic, M.; Milosevic, S. D., Frenkel's Theory of Sintering. *Science of Sintering* **2006**, 38 (1), 7-11.
54. William, D. (2001). *Fundamentals of Materials Science and Engineering*. The United States of America: The University of Utah.
55. Muralithran, G.; Ramesh, S., The Effects of Sintering Temperature on the Properties of Hydroxyapatite. *Ceramics International* **2000**, 26 (2), 221-230.
56. Bai, J. G.; Zhang, Z. Z.; Calata, J. N.; Lu, G., Low-Temperature Sintered Nanoscale Silver as a Novel Semiconductor Device-Metallized Substrate Interconnect Material, *IEEE Transactions on Components and Packaging Technologies*, **2006**, 589-593.
57. Grouchko, M.; Kamyshny, A.; Mihailescu, C. F.; Anghel, D. F.; Magdassi, S., Conductive Inks with a "Built-In" Mechanism That Enables Sintering at Room Temperature. *ACS Nano* **2011**, 5 (4), 3354-3359.

58. Yati, I.; Ridwan, M.; Jeong, G. E.; Lee, Y.; Choi, J. W.; Yoon, C. W.; Suh, D. J.; Ha, J. M., Effects of Sintering-Resistance and Large Metal–Support Interface of Alumina Nanorod-Stabilized Pt Nanoparticle Catalysts on The Improved High Temperature Water Gas Shift Reaction Activity. *Catalysis Communications* **2014**, *56*, 11-16.
59. Yentekakis, I. V.; Goula, G.; Panagiotopoulou, P.; Kampouri, S.; Taylor, M. J.; Kyriakou, G.; Lambert, R. M., Stabilization of Catalyst Particles Against Sintering on Oxide Supports With High Oxygen Ion Lability Exemplified by Ir-Catalyzed Decomposition of N<sub>2</sub>O. *Applied Catalysis B: Environmental* **2016**, *192*, 357-364.
60. Wang, Z. (2011). *Polydimethylsiloxane Mechanical Properties Measured by Macroscopic Compression and Nanoindentation Techniques*. The United States of America: University of South Florida.
61. Carmichael, N., Linear-Polydimethylsiloxanes. *Joint Assessment of Commodity Chemicals* **2011**, 1-155.
62. Camino, G.; Lomakin, S. M.; Lazzari, M., Polydimethylsiloxane Thermal Degradation Part 1. Kinetic Aspects. *Polymer* **2001**, *42* (6), 2395-2402.
63. Welch, C. M.; Banks, C. E.; Simm, A. O.; Compton, R. G., Silver Nanoparticle Assemblies Supported on Glassy-Carbon Electrodes for the Electro-Analytical Detection of Hydrogen Peroxide. *Analytical and Bioanalytical Chemistry* **2005**, *382* (1), 12-21.
64. Ye, Y.; Xiao, H.; Reaves, K.; McCulloch, B.; Mike, J. F.; Lutkenhaus, J. L., Effect of Nanorod Aspect Ratio on Shear Thickening Electrolytes for Safety-Enhanced Batteries. *ACS Applied Nano Materials* **2018**, *1* (6), 2774-2784.
65. Tsentalovich, D. E.; Headrick, R. J.; Mirri, F.; Hao, J.; Behabtu, N.; Young, C. C.; Pasquali, M., Influence of Carbon Nanotube Characteristics on Macroscopic Fiber Properties. *ACS Applied Materials & Interfaces* **2017**, *9* (41), 36189-36198.
66. Tohru, K.; Masayoshi, K., Diffuse Reflectance Infrared Fourier Transform Spectra of Solid Silver Acetate. *Kitami Institute of Technology Research Report* **2019**, *15*, 169-175.
67. Martina, I.; Wiesinger, R.; Jembrih Simburger, D.; Schreiner, M., Micro-Raman Characterization of Silver Corrosion Products: Instrumental Set-Up and Reference

- Database. **2012**, 9, 1-6.
68. Fathollahi, M.; Pourmortazavi, S. M.; Hosseini, S. G., Particle Size Effects on Thermal Decomposition of Energetic Material. *Journal of Energetic Materials* **2007**, 26 (1), 52-69.
69. Yang, H.; Nguyen, Q. T.; Ding, Y.; Long, Y.; Ping, Z., Investigation of Poly(dimethyl Siloxane) (PDMS)–Solvent Interactions by DSC. *Journal of Membrane Science* **2000**, 164 (1), 37-43.
70. Corning, D. (2014). *PDMS Dow Corning 184 Properties*. The United States of America: Dow Corning Corporation.
71. Brewer, B.; Gao, Y.; Li, D., A Study of Small Molecule Absorption in Polydimethylsiloxane, **2012**, 15-19.
72. González, R. J.; Iglío, R.; Barillaro, G.; Duce, C.; Tinè, M., Structural and Thermoanalytical Characterization of 3D Porous PDMS Foam Materials: The Effect of Impurities Derived from a Sugar Templating Process. *Polymers* **2018**, 10 (6), 616-628.
73. Mehta, S. K.; Chaudhary, S.; Gradzielski, M., Time Dependence of Nucleation and Growth of Silver Nanoparticles Generated by Sugar Reduction in Micellar Media. *Journal of Colloid and Interface Science* **2010**, 343 (2), 447-453.
74. Kawaguchi, M., Silicone Oil Emulsions Stabilized by Polymers and Solid Particles. *Advances in Colloid and Interface Science* **2016**, 233, 186-199.
75. Han, Z.; Fina, A., Thermal Conductivity of Carbon Nanotubes and Their Polymer Nanocomposites: A Review. *Progress in Polymer Science* **2011**, 36 (7), 914-944.
76. Kapadia, R. S.; Louie, B. M.; Bandaru, P. R., The Influence of Carbon Nanotube Aspect Ratio on Thermal Conductivity Enhancement in Nanotube–Polymer Composites. *Journal of Heat Transfer* **2013**, 136 (1), 11303-11306. doi: 10.1115/1.4025047
77. Tekce, H. S.; Kumlutas, D.; Tavman, I. H., Effect of Particle Shape on Thermal Conductivity of Copper Reinforced Polymer Composites. *Journal of Reinforced Plastics and Composites* **2016**, 26 (1), 113-121.



จุฬาลงกรณ์มหาวิทยาลัย  
**CHULALONGKORN UNIVERSITY**

## VITA

**NAME** Porapak Suriya

**DATE OF BIRTH** 3 Sep 1993

**PLACE OF BIRTH** Angthong

**INSTITUTIONS ATTENDED** Department of Chemistry, Faculty of Science and Technology, Thammasat University

**HOME ADDRESS** 24/18 Tedsabal 5 road T.Taladluang A.Meung Angthong 14000

**PUBLICATION** Kongparakul, S.; Kornprasert, S.; Suriya, P.; Le, D.; Samart, C.; Chantarasiri, N.; Prasassarakich, P.; Guan, G., Self-healing hybrid nanocomposite anticorrosive coating from epoxy/modified nanosilica/perfluorooctyl triethoxysilane. Progress in Organic Coatings 2017, 104, 173-179.